Physics of the Earth and Planetary Interiors 366 (2025) 107383

Contents lists available at ScienceDirect

Physics of the Earth and Planetary Interiors

journal homepage: www.elsevier.com/locate/pepi

Porosity and hydrous alteration of the Martian crust from InSight seismic data☆

Brigitte Knapmeyer-Endrun [a,*], Ludmila Adam [b], Sebastian Carrasco [c,1], Matthew P. Golombek [d], Doyeon Kim [e], Martin Knapmeyer [f], Katarina Miljković [g], Ana-Catalina Plesa [f], Nicholas H. Warner [h], Mark Wieczorek [i]

[a] Microgravity User Support Center, Deutsches Zentrum für Luft - und Raumfahrt, Linder Höhe, 51147 Köln, Germany
[b] School of Environment, Faculty of Science, The University of Auckland, Auckland 1010, New Zealand
[c] Bensberg Observatory, University of Cologne, 51429 Bergisch Gladbach, Germany
[d] Jet Propulsion Laboratory, California Institute of Technology, Pasadena, CA, USA
[e] Department of Earth Science and Engineering, Imperial College London, South Kensington Campus, London SW7 2AZ, United Kingdom
[f] Institute of Planetary Research, Deutsches Zentrum für Luft- und Raumfahrt, Rutherfordstrasse, 12489 Berlin, Germany
[g] School of Earth and Planetary Sciences, Space Science and Technology Center, Curtin University, Perth, WA, Australia
[h] Department of Geological Sciences, State University of New York at Geneseo, Geneseo, NY, USA
[i] Université Paris Cité, Institut de Physique du Globe de Paris, CNRS, 75005 Paris, France

ARTICLE INFO

Keywords:
Mars
Crust
Rock physics
Porosity
Water
Ice

ABSTRACT

The composition and layering of the Martian crust provide important constraints on planetary crustal evolution as well as on present-day conditions, e.g., with regard to the presence of liquid water or ice. The seismic data of the InSight mission yielded new and critical information on crustal structure at several locations on Mars. Here, we use rock physical models to investigate the range of lithologies, porosities and alteration scenarios compatible with seismic P- and S-wave velocities as well as v_P/v_S ratios from InSight. We find that present-day crustal porosity extends to 20–25 km depth at all sampled locations, with large Noachian impacts as main drivers for the creation of porosity, and viscous pore closure as likely agent of removal of porosity at depth, resulting in a discontinuous increase in seismic velocities. Spatially heterogeneous seismic velocities can be related to differences in porosity that could be caused by subsequent localized magmatic activity. At the InSight landing site, where seismic data indicate a four-layered crust, hydrated minerals as traces of aqueous alteration are present throughout the crust, though the water within these minerals could be fairly limited at 0.3 wt% or less. The most likely types of hydrated minerals are also consistent with a post-depositional environment that was limited in water. The velocity increase at about 10 km depth beneath InSight can either be attributed to a change in composition from felsic to basaltic, or to a change in porosity by the deposition of Utopia ejecta. A felsic component to the crust, e.g. due to impact-generated buoyant partial melts, can accordingly not be excluded, but would not be present globally. Seismic and geological constraints for the layer at approximately 200 m to 2000 m depth beneath the lander strongly favor basaltic Noachian sediments saturated with a mixture of up to 10 % ice and brine. However, the lateral extent of this present day aquifer is not constrained by the available data.

1. Introduction

Using data from the SEIS (Seismological Experiment for Interior Structure) instrument (Lognonné et al., 2019), the InSight mission has provided the first in-situ seismological constraints on the interior structure of Mars (Banerdt et al., 2020), from the near surface to the core. These included measurements of crustal velocities, layering, and thickness that can be analyzed in terms of rock physical properties, for example lithology, porosity, and pore-filling medium. These parameters have direct implications for the crustal formation and evolution of Mars

☆ This article is part of a Special issue entitled: 'Mars Interior' published in Physics of the Earth and Planetary Interiors.

* Corresponding author.
E-mail address: brigitte.knapmeyer-endrun@dlr.de (B. Knapmeyer-Endrun).
[1] Now at: Institute for Geology, Mineralogy and Geophysics, Ruhr-University Bochum, 44801 Bochum, Germany.

https://doi.org/10.1016/j.pepi.2025.107383
Received 28 June 2024; Received in revised form 16 May 2025; Accepted 16 May 2025
Available online 29 May 2025

as well as for the past and present existence of ice or liquid water in the crust. Since the Martian crust has not been affected by plate tectonics and is in larger parts Hesperian or older, it preserves information on early planetary conditions and processes that is not accessible e.g. on Earth.

While initial investigations of the Martian crust focused on the local structure at the InSight landing site, data from later marsquakes, specifically those at a larger distance to SEIS and those with larger magnitudes, also provided constraints on the crustal structure away from the lander, and on a more regional or even global scale. The current seismic information on crustal structure is summarized in Fig. 1 and described in more detail below.

1.1. Landing site

The InSight lander is located in western Elysium Planitia near the dichotomy boundary (Fig. 1), on smooth plains consisting of Early Amazonian to Hesperian basaltic lava flows which are around 200 m thick (Golombek et al., 2018, 2020). The lavas are likely vesicular and highly fractured due to thermal cooling at the outer surface, rotational

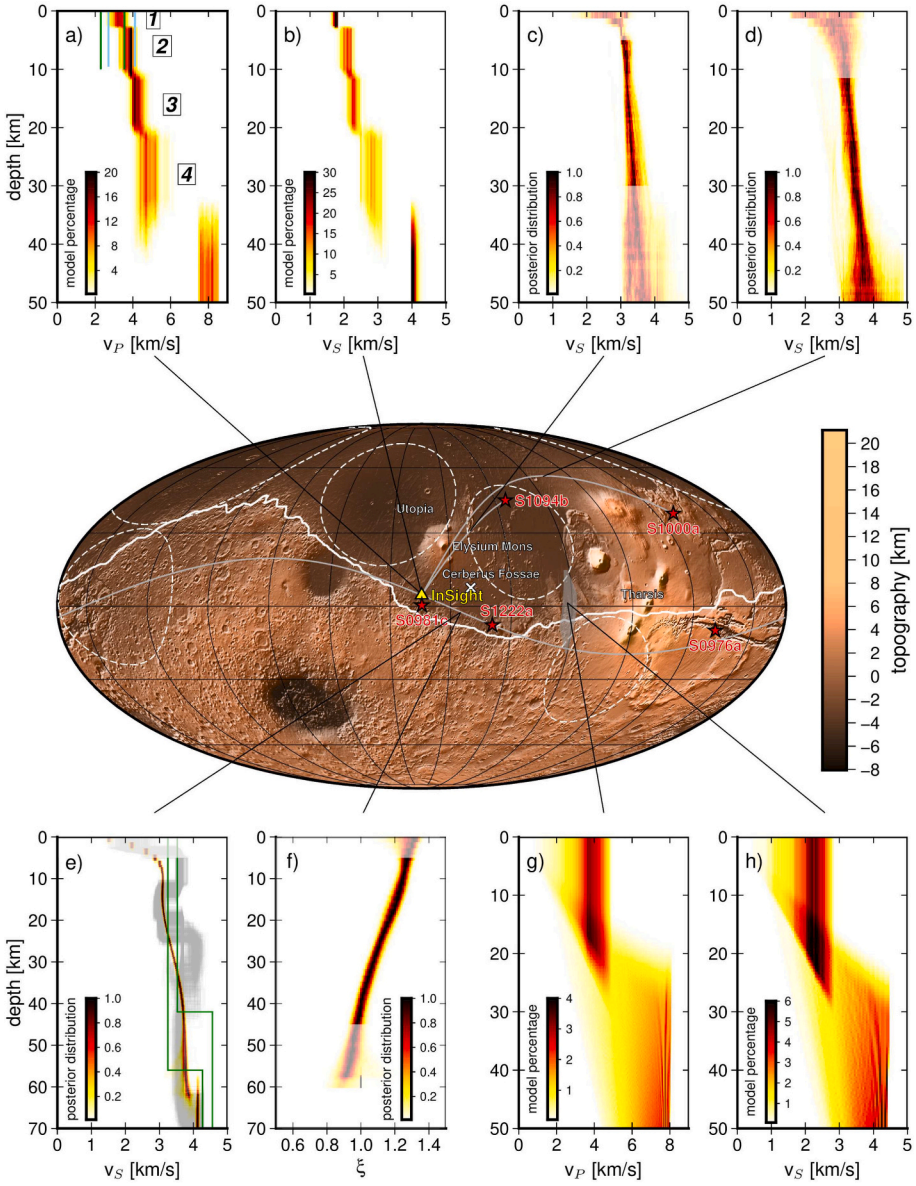

Fig. 1. Selected crustal velocity models based on InSight data. The central map shows locations of InSight and some seismic events discussed in the text (red stars with labels), as given by the MarsQuake Service (InSight Marsquake Service, 2023), overlain on MOLA topography (Smith et al., 2003). The best-fit location of the plume head of the Elysium Planitia plume suggested by Broquet and Andrews-Hanna (2023) is indicated by a white X. The dichotomy boundary (white line) is based on Andrews-Hanna et al. (2008). The white dashed circles outline the diameters of the five largest Noachian impact basins (Roberts and Arkani-Hamed, 2012). a) and b) show P- and S-wave velocity models for the landing site from Carrasco et al. (2023b). Green lines in a) indicate independent constraints on P-wave velocities from Li et al. (2023a), whereas light blue lines indicate 2 σ P-wave velocities from 3D-RF stacking (Kim et al., 2021). c) and d) show S-wave velocity models along great circle arcs between InSight and events S1094b and S1000a (gray lines on the map) from Kim et al. (2022). In e) and f), colour coded models show S-wave velocities and anisotropy along the great circle arc between InSight and event S1222a from Kim et al. (2023b), whereas gray lines in the background of e) depict alternative isotropic models from Xu et al. (2023). Green lines outline the range of velocities averaged along the great circle through InSight and the event around the whole planet (Kim et al., 2023a). g) and h) show P- and S-wave velocity profiles at the bounce point of event S0976a, and possible bounce point locations are indicating by gray shading in the map, from Li et al. (2022a). (For interpretation of the references to colour in this figure legend, the reader is referred to the web version of this article.)

stresses at the flow front (Hanna and Phillips, 2005), and subsequent impacts. Identification of clay and sedimentary rocks in the basement underneath the basalts provides evidence for aqueous processes, which could also have affected the landing site (Pan et al., 2020; Warner et al., 2022). Seismically, the fine structure in the shallowest part of the crust below InSight has been resolved down to about 200 m depth, mainly constraining S-wave velocities, and shows layering interpreted as intercalation of low-velocity sediments with higher-velocity lava flow units of Amazonian and Hesperian age, respectively (Hobiger et al., 2021; Carrasco et al., 2023a). This shallow part is not discussed further in this study, which focuses on the crust at kilometer-depth-scales. The Noachian-age crust below the Hesperian strata is expected to be heavily cratered in general (Frey et al., 2002). Topographic data also suggests that older Noachian craters could be buried beneath the volcanic plains in the InSight landing region (Golombek et al., 2018). Accordingly, the Noachian-age crust could contain a significant amount of impact-generated porosity.

At a larger scale, low SV-velocities in the uppermost approximately 10 km of the crust beneath InSight were derived early on, based on P-to-S receiver functions (RFs) from only two marsquakes (Lognonné et al., 2020). Analysis of SH-reflections (Li et al., 2022b) as well as SsPp phases (Li et al., 2023a) confirmed a strong impedance contrast approximately 10 km deep beneath the lander. The timing of the SH-reflections requires lower SH- than SV-velocities in the layer above, consistent with radial anisotropy caused by east-west oriented fractures or intrusions (Li et al., 2022b). The SsPp study put additional constraints on the P-wave velocity in the uppermost 10 km (Li et al., 2023a), which is not well constrained by RFs.

Data from additional events constrained the crustal structure at the landing site, specifically in terms of S-wave velocities, down to the crust-mantle boundary at around 40 km depth based on RFs, with crustal discontinuities at around 10 and 20 km depth (Knapmeyer-Endrun et al., 2021; Kim et al., 2021; Durán et al., 2022). While initial results were compatible with two distinct crustal thicknesses (Knapmeyer-Endrun et al., 2021), crustal thickness at the landing site was later uniquely constrained by the use of additional converted phases (PPs and Sp) by Kim et al. (2021). The derived layering is also broadly consistent with signals observed in vertical component autocorrelations, which provide independent constraints on P-wave velocities (Knapmeyer-Endrun et al., 2021; Schimmel et al., 2021; Compaire et al., 2021). Though the RF-based studies generally parameterized their velocity models in v_S and v_P/v_S (Knapmeyer-Endrun et al., 2021; Durán et al., 2022; Dai and Sun, 2023), studies that explicitly utilized the arrival times of multiple reflected and converted phases additionally provided tighter, independent constraints on the v_P/v_S ratios of the crustal layers (Kim et al., 2021; Joshi et al., 2023).

Based on these results, Wieczorek et al. (2022) used gravity and topography data to deduce that the crustal density of Mars should be significantly lower than the mineral density of iron-rich basalts (the presumed main constituent of the upper crust) and proposed a number of scenarios to explain the observed crustal layering, which are described in more detail at the beginning of section 5. Rock physics modeling can help to further differentiate between these scenarios.

Subsequently, Shi et al. (2023) reported evidence of a shallow crustal layer of around 2 km thickness beneath InSight from modeling high-frequency RFs. The existence of this layer has been confirmed independently by Carrasco et al. (2023b), Drilleau et al. (2023) and Dai and Sun (2023). Dai and Sun (2023) were mainly able to constrain S-wave velocities and showed that a gradational velocity increase in the topmost layer, rather than a layer with a constant velocity, is also possible. In a similar fashion, Mun and Kim (2024) modeled a stepwise increase in P- and S-wave velocities within the uppermost 2500 m beneath InSight, based on amplitude ratios of the P-wave arrival. Carrasco (2024) found that a velocity gradient between 200 m and 2000 m depth in S-wave velocities is actually required to simultaneously fit horizontal-to-vertical spectral ratios of InSight event codas, including event S1222a (the largest marsquake recorded by InSight), the Rayleigh wave ellipticity of S1222a, and RF waveforms.

In summary, the crustal structure beneath the landing site below about 200 m depth consists of four layers, in the following named layer 1 to 4 from top to bottom, with boundaries at about 2 km, 10 km, 20 km depth and the Moho at around 40 km depth (Fig. 1a,b). A gradual velocity increase is required within layer 1, whereas constant velocities within the other layers are sufficient to fit the data. As the landing site models are mostly based on RFs, S-wave velocities are primarily constrained, with secondary constraints on v_P/v_S ratios for studies that consider multiple reflected phases (Kim et al., 2021; Joshi et al., 2023). The only crustal-scale inversion that explicitly included P-wave reverberations and thus provides tighter constraints on P-wave velocities than the purely RF-based inversions is Carrasco et al. (2023b). Still, in absolute values, the bounds on S-wave velocities are in all studies tighter than those on P-wave velocities. Velocities in all four layers are comparatively low, with S-wave velocities clearly below 3 km/s to at least 20 km depth.

Analysis of local impact signals (Garcia et al., 2022) provided the first constraints on the extent of this velocity structure around InSight. These observations imply that higher crustal velocities dominate differential travel-time measurements that average over 250 km distance from InSight (i.e. along the ray path to impact S0981c), whereas the landing site model can well explain differential travel-time measurements taken within 100 km of the lander (Menina et al., 2023; Drilleau et al., 2023).

1.2. Regional to global scale

Surface waves from two giant impacts, S1094b and S1000a, which formed the largest ever detected fresh impact craters on present-day Mars (Posiolova et al., 2022; Dundas et al., 2023), and S1222a, the largest marsquake recorded by InSight, allowed crustal properties away from the landing site to be constrained (Kim et al., 2022; Beghein et al., 2022; Li et al., 2023b; Xu et al., 2023; Kim et al., 2023b), and, using multi-orbit Rayleigh waves of S1222a, even globally (Kim et al., 2023a). Both impact craters are located northeast of InSight, whereas S1222a is located to the southeast, near the dichotomy boundary. The relatively high uncertainty in the backazimuth determination of S1222a implies that the event could in fact be located south of the dichotomy (Kim et al., 2023a; Carrasco et al., 2023b; Maguire et al., 2023). In any case, the great circle through InSight and S1222a, along which multi-orbit surface waves propagate, runs to a large extent through highland terrain (see e.g. Fig. 1 in Kim et al., 2023b).

All surface wave inversions only constrain S-wave velocities, with no information on P-wave velocities or v_P/v_S ratios. Results indicate distinctly higher SV-velocities than those found in the uppermost 20 km beneath the InSight lander. Velocities derived from S1094b and S1000a, that partly cover the same ray path, show good agreement (Kim et al., 2022). Data from S1222a shows a Love-Rayleigh discrepancy that can either be explained by radial anisotropy in the 5 km to 30 km depth range (Beghein et al., 2022; Kim et al., 2023b), or by an isotropic model consisting of a distinct high-velocity layer between about 2 and 12 km depth, overlying lower velocities that extend 20 to 25 km deep (Xu et al., 2023). The scale of these layers is smaller than the wavelengths of the surface waves considered, and thus consistent with velocity layering as a proposed explanation for the radial anisotropy (Beghein et al., 2022).

The cause of the Martian crustal dichotomy and whether densities - and shear wave velocities - are the same in the northern lowlands and the southern highlands has long been debated. Constraints by InSight are given in a study that used multi-orbit Rayleigh waves from S1222a, combined with global crustal thickness modeling using gravity and topography data, to limit the density contrast between the lowlands and highlands to200 kg/m^3 or less, with lower densities (and hence velocities) in the south (Kim et al., 2023a).

The most distant marsquake located with InSight, S0976a, allowed

the observation of precursory phases to both the PP and SS arrivals, which constrain the crustal structure at the bounce point located near the equator (Fig. 1). Whereas the existence of layering within the uppermost 25 km of the crust at that location could neither be confirmed nor ruled out, and the derived velocity models have a comparatively large uncertainty, velocities within that depth range are compatible with those found at the landing site (Li et al., 2022a). The required S-wave velocities below 2.8 km/s and P-wave velocities below 4.5 km/s are neither compatible with the models based on surface wave dispersion (Kim et al., 2023b) nor with the crustal velocities required to explain the differential travel-time of impact S0981c, 250 km to the south of InSight (Drilleau et al., 2023; Menina et al., 2023), though. This makes it unlikely that these low velocities persist over a continuous region between InSight and the bounce point location. Note that PP and SS precursor arrival times were inverted separately by Li et al. (2022a) to generate two separate sets of velocity models, so there is no information on v_P/v_S ratios at the bounce point.

1.3. Previous rock physics models

The influence of the pore-filling medium on seismic velocities of porous basalts has first been pointed out in the context of InSight by Heap (2019). The initial results of low SV-velocities in the uppermost 10 km beneath the InSight lander (Lognonné et al., 2020) have been used to exclude a thick, ice-saturated cryosphere at this location (Manga and Wright, 2021), based on modeling of elastic moduli in porous basalt. Wright et al. (2022) used rock physics models for sediments as well as fractured basalts to interpret selected velocity models of the uppermost 300 m beneath InSight (Hobiger et al., 2021), whereas Kilburn et al. (2022a) employed the same approach to explain SV-velocities of early crustal models (Knapmeyer-Endrun et al., 2021) to 20 km depth beneath the lander. Recently, both Wright et al. (2024) and Katayama and Akamatsu (2024) provided rock physics models for mid-crustal depths (layer 3) at the landing site. Both studies suggest water saturation of that layer to explain seismic velocities, and their sudden increase in approximately 10 km depth, though they disagree about the specifics: When considering dry vs. water-saturated cracked basalts, Katayama and Akamatsu (2024) show that the pore aspect ratio favored by Wright et al. (2024) does not lead to the required sudden velocity increase around 10 km depth, whereas the aspect ratios used in their study are not within the range considered by Wright et al. (2024). The two studies also try to fit different seismic constraints from the literature, with a more consistent selection by Katayama and Akamatsu (2024).

With the exception of the latter two studies, rock physics studies at crustal scales have not considered P-wave velocities or v_P/v_S ratios. SV-, SH- and P-wave velocities of the uppermost 10 km beneath the lander have been interpreted individually and independently in terms of porosity in the respective studies deriving those velocities. However, a rock physics interpretation combining P- and S-wave velocities and v_P/v_S ratios across the whole crustal range, and including the additional layer boundary at about 2 km depth below InSight, as well as a comparison to other parts of the planet, is still missing.

In section 2, we provide a brief summary of the theoretical background of the rock physics models, while section 3 discusses the lithologies we consider, and which additional information is available to e.g. constrain the presence of water in the crust. More details can be found in Supplementary Texts S1-S6. Section 4 describes the results of comparing a variety of model outputs with the seismic constraints, with a major focus on the landing site, for which the best information is available. Section 5 discusses these results and a probable scenario for crustal evolution in light of information from geology, lithology and thermal evolution models. The results are summarized in Table 2 and in section 5.5 in terms of a composite model for the landing site. Based on this, section 5.6 describes the resulting density structure of the crust and provides estimates of the amount of water sequestered in the crust.

2. Theory

For the upper crust (i.e. down to about 10 km depth at the landing site), we consider both models for porous sediments and sedimentary rocks as well as cracked igneous rocks. Fine-grained sediments - either due to aeolilan, volcanic or ancient fluvial deposition - are most likely in the uppermost part of the crust, so we only consider this model relevant for layers 1 and 2 (Wilson and Head III, 1994; Taylor and McLennan, 2009). While the main points and references for each theory are given here, a more detailed discussion including the implemented equations can be found in the supporting information (Supplementary Texts S1-S5).

2.1. Sediments and sedimentary rocks

Following the approach by Wright et al. (2022), we use the Hertz-Mindlin model to describe unconsolidated dry sediments (Mindlin, 1949), and assume an exponential decrease of porosity with depth due to compaction (Rubey and King Hubbert, 1959). Bachrach and Avseth (2008) extended the Hertz-Mindlin model to non-uniform grain contacts with associated heterogeneities in stress by using a binary mixture model. In this model, some grain contacts are smooth with zero tangential stiffness, i.e. resistance against tangential slip or friction, and some contacts have finite tangential stiffness, or friction, as in the original Hertz-Mindlin model. The tangential stiffness only affects the shear modulus, with two end member cases where all grain contacts show either perfect adhesion (rough grain contacts), or can be described by absolutely friction-less spheres (smooth grain contacts). In addition to the relative amount of (rough) grain contacts with finite tangential stiffness, other variables in this model are the porosity at the surface ϕ_0 (depositional porosity) and the materials considered (i.e. elastic moduli of the grains and the pore-filling material).

For consolidated sedimentary rocks, we use the cemented-sand model by Dvorkin and Nur (1996), which allows us to estimate the effective bulk and shear moduli of dry sand with cement deposited at grain contacts (Mavko et al., 2020). Dvorkin and Nur (1996) introduced two end-member schemes representing the stiffest and softest bounds for cement deposition, by either depositing all cement at grain contacts or evenly across the grain surfaces. Allo (2019) extended the corresponding equations to also model mixtures between the two end members, i.e. intermediate deposition schemes, by introducing the cement cohesion coefficient. In addition to this coefficient, free parameters are again the depositional porosity and the materials considered for grains, cement, and pore-filling medium.

The effect of water instead of the atmosphere filling the pores is estimated using low-frequency Gassmann-Biot theory (Gassmann, 1951; Biot, 1956). In this theory, the exchange of pore fluids has no influence on the shear modulus, which has also been confirmed in lab experiments (Hatakeyama et al., 2021).

2.2. Cracked or porous rocks

Simple rock physics theories that do not consider the shapes of cracks and pores can only provide bounds on elastic parameters for the effective composite medium, but these bounds lie far apart if the properties of the pore filling medium differ significantly from those of the background medium, as is the case for fluids or gas (Berge et al., 1992). To provide better estimates, a number of different models that include the shape of

the inclusions are available. They are all based on the strain concentration tensor for a single elastic ellipsoid in an infinite, uniform, elastic background medium (Eshelby, 1957), but Berge et al. (1993) showed that at moderate to high porosities, the different theoretical approaches predict different velocities (see also Supplementary Figs. S3 and S4).

We use differential effective medium theory (DEM, Norris, 1985; Berryman et al., 2002) to model InSight velocity information. DEM models a two-phase composite by incrementally adding inclusions of the second phase to a background medium, which initially consists purely of the first phase and is updated at each step by adding a new increment of the second phase. In this way, the theory is exploiting the accuracy of the Eshelby model at very dilute concentrations. While other theories might work better for sedimentary rocks with a granular microstructure such as sandstones, DEM has been found to be more accurate for estimating velocities of rocks like basalts with isolated cracks or pores (Berge et al., 1993). The theory has been applied on Earth to model basaltic oceanic crust with porosities of up to 30 % (Berge et al., 1992; Arnulf et al., 2011). An advantage of DEM in comparison to the self-consistent models of Berryman (1980) that have previously been applied to model InSight data (e.g. Wright et al., 2022; Kilburn et al., 2022a) is that only the aspect ratio α of the inclusions is required and no assumption regarding the aspect ratio of the background medium has to be made (Supplementary Fig. S3). Assuming different aspect ratios for the background medium has a significant effect on the resulting velocities. For the example of cracked or porous basalt with CO_2-filled pores, S-wave velocities differ by up to 2 km/s, and P-wave velocities by up to 3 km/s when assuming an aspect ratios of 1 versus 0.1 for the background medium (Supplementary Fig. S4 and associated text). As this parameter is poorly constrained for the martian crust and DEM results shows good agreement with other theories in the mutually covered parameter space (Supplementary Figs. S3, S4 and associated text), we chose to use DEM.

Variables in DEM are the porosity, the crack aspect ratio, and the elastic moduli of the materials considered for the background medium and pores.

The effect of fluids in the pores or cracks is again estimated using low-frequency Gassmann-Biot theory (Gassmann, 1951; Biot, 1956). A composite model is needed if more than one phase is assumed to fill the pores or cracks, e.g. due to deposition of ice or precipitation of secondary minerals, resulting in veins as observed in Martian meteorites (Bridges et al., 2001). A common approach is to replace the composite by an effective particle, i.e. a new, uniform-property particle of the same size as the composite, that is then used to model an inclusion (e.g. in DEM). Explicit analytical expressions for the effective particle have been provided for the case of spherical core-shell particles (Christensen, 1990; Garboczi and Berryman, 2001). Since, to the best of our knowledge, no comparable expressions are available for spheroids in 3D, we use the equation for spherical inclusions in the DEM to model secondary mineral precipitation in the pore space. Spherical inclusions result in higher velocities as compared to elliptical cracks with a small aspect ratio; hence, the velocities derived for spherical core-shell particles that we use here will likely overestimate velocities for coated elliptical cracks. Still, the approximation by spherical inclusions is considered more accurate, especially for small amounts of coating, than the use of an upper bound like the Voigt average (Supplementary Figs. S5, S6), as done in previous studies (Wright et al., 2022; Kilburn et al., 2022a, 2022b). The Voigt average provides estimates for the velocity of the inclusion that are nearly independent of the amount of coating (Supplementary Fig. S5). Differences in the seismic velocities of the modeled cracked rock of up to 20 % between the two methods for averaging the coating are possible for a lithology relevant to this study (Supplementary Fig. S6).

2.3. Anisotropy

Following Li et al. (2022a), we use the effective medium solution for the elasticity matrix (Tandon and Weng, 1984) as implemented in the MSAT package (Walker and Wookey, 2012) to model azimuthal anisotropy in the upper crust at the landing site. We consider cracks with a horizontal symmetry axis to obtain transverse isotropy and use our DEM-derived elastic parameters for the background medium to which these cracks are added. We focus on cracks and do not consider igneous intrusions, which were also studied by Li et al. (2022a), or other sources of anisotropy, since cracking in layer 2 is already required to explain the low observed velocities (see section 4.1.2), and adding intrusions would have the opposite effect of increasing velocities. For the cracks, we assume the same mixture between pore filling and coating, and use the same equations for effective particles as above to calculate their effective elastic parameters. Note that there is a trade-off between the influence of volume fraction of cracks and their aspect ratio on the anisotropy coefficient ξ, and we choose these values to be consistent with values that fit isotropic velocities and v_P/v_S ratios in the corresponding layer. Quasi-SV and -SH speeds, and ξ from them, are determined by solving the Christoffel equation. Since the RFs used to derive the models are predominantly calculated from marsquakes in Cerberus Fossae, we use an incidence angle of 20°, as in Li et al. (2022a), that is appropriate for epicentral distances of around 30° on Mars.

3. Considered parameters and lithologies

3.1. Porosity

3.1.1. Sediments and sedimentary rocks

For sediments and sedimentary rocks, the depositional porosity at the surface is often equated with the critical porosity, above which the sediment can exist only as a suspension and the stiffness of the sediment is determined by the pore fluid and not the framework of contacting grains (Dvorkin and Nur, 2002). Critical porosities for sandstones, limestones, dolomites, rock salt, and sintered glass beads are 40 % (Nur et al., 1998), but values up to 50 % are observed for terrestrial sands, whereas slightly larger values of up to 55 % were determined for the Mars simulants MSS-D and MMS sand (Becker and Vrettos, 2016). Referring to typical values for sands, we vary depositional porosity between 30 % and 50 % in our calculation for sediments and sedimentary rocks, which also brackets the value of 40 ± 6 % porosity derived for sediments in Gale crater from in situ measurements (Lewis et al., 2019).

3.1.2. Cracked or porous rocks

In contrast to the compaction-related exponential decrease of porosity with depth in sediments, terrestrial studies are more ambiguous regarding changes of porosity with depth in crystalline bedrock above the brittle-ductile transition (e.g. Ferguson et al., 2021, and references therein). Though some studies assume constant porosity with depth, pores and cracks will generally close with increasing pressure (Wilson and Head III, 1994), with an additional dependence on aspect ratio (Walsh, 1965, Supplementary Fig. S9). When considering impact bombardment as the main mechanism that creates cracks, it is reasonable to assume that the larger amount of smaller impactors will preferentially increase the crack density at shallower depth in the first place (Branco et al., 2024). However, in all considered rock physics models, a decrease of porosity will lead to an increase in velocity (Supplementary Fig. S3). Apart from layer 1, no velocity increase with depth within specific layers is resolved or required by the seismic data for the landing site. In theory, a simultaneous decrease in aspect ratio with depth could counteract the velocity effect of decreasing porosity (Supplementary Fig. S3), but this is contrary to expectations (Walsh, 1965, Supplementary Fig. S9). Accordingly, this effect is neglected here and we model porosity as constant within each of the crustal layers.

MacKinnon and Tanaka (1989) suggest porosities of 10 to 20 % as realistic for the near-surface layer on Mars, i.e. a megaregolith breccia of consolidated impact ejecta. Hanna and Phillips (2005) model around 5 % porosity below that layer, in the heavily fractured and partially brecciated basement. In contrast, Goossens et al. (2017) need an average

Martian crustal porosity of 10 to 23 % to explain the low crustal densities they derive from gravity inversions when assuming a basaltic composition.

Hanna and Phillips (2005) argue that the brittle-to-plastic transition as well as pressure solution and mineral precipitation are the primary mechanism of reducing porosity to zero at depth, and not elastic pore closure. Furthermore, they deduce that viscous closure of pores and cracks (Gyalay et al., 2020), which is strongly temperature-dependent, affected the Noachian crust at depths below 10 to 20 km. In contrast, De Toffoli et al. (2021) suggested that pervasive deep cracking reaches up to 55 km depth in Arcadia Planitia, based on the interpretation of pitted mounds in that region as eruption centers for fluid and sediment resurgences.

Based on the above, and to allow for porosity in individual layers to reasonably deviate from the crustal average, we consider porosities between 0 and 35 % across the whole crustal depth range in our modeling.

3.2. Crack aspect ratios

Even a minor contribution of cracks with small aspect ratios to the porosity has a profound effect on velocities (Wilkens et al., 1991; Berge et al., 1992), but cracks with the lowest aspect ratios are also the first to be sealed by alteration or closed by compression. This potentially results in increasing velocities coupled to an only small reduction in total porosity (Wilkens et al., 1991). We use the model by Walsh (1965), in which the pressure required to close a crack is proportional to the Young's modulus times the crack's aspect ratio, to estimate the minimum aspect ratio with depth (Supplementary Fig. S9). Cracks with aspect ratios of 0.001 are possible to at most 8 km depth, in case of low porosity, whereas cracks with aspect ratios of 0.01 can exist at 15 km to more than 20 km depth. Note that, according to this model, for cracks with the aspect ratios assumed by Katayama and Akamatsu (2024) for layer 3 at the landing site, the closure depth might actually be less than 20 km. In our modeling, we consider aspect ratios between 1 (spherical) and 0.001, which includes the ranges considered by both Wright et al. (2024) and Katayama and Akamatsu (2024), to also encompass the possible range in the uppermost part of the crust.

3.3. Considered lithologies

3.3.1. Host rock

Information on Martian crustal composition is provided by SNC meteorites, orbital (spectroscopic) measurements and in situ measurements at robotic landing sites. Based on these data, Mars' upper crust is considered to be primarily basaltic, though other rock types have been found as well (e.g. Taylor et al., 2008). Following an analysis of gravity and topography data that indicates that the density of both the Elysium volcano and the underlying crust is the same (Belleguic et al., 2005), the entire northern lowland crust may be largely basaltic. However, recent evidence of feldspar-dominated rocks of Noachian age (e.g Bandfield et al., 2004; Sautter et al., 2016; Payré et al., 2022) as well as identification of gabbro in SNC meteorites (Udry et al., 2020) led us to also consider mineralogical boundaries with a rock made only of plagioclase as the felsic end member and a gabbro as the mafic end member.

3.3.2. Cements and coating

Regarding cements and coating, Fe/Mg phyllosilicates, i.e. clays, are the most widespread hydrated minerals on Mars (Poulet et al., 2005; Sun and Milliken, 2015), specifically in Noachian outcrops. For the northern lowlands, the study of bedrock as excavated by impact craters indicates infilling by about 2 km of volcanic materials above a hydrated basement containing e.g. Fe/Mg smectites, chlorite or hydrated silica, but no widespread carbonates, like calcite, or other evaporative salts (Pan et al., 2017). Evidence from uplifted rocks in crater central peaks suggests that clays exist to depths of at least 7 km below the surface in the Martian crust, and chlorites may have been excavated from approximately 17 km depth (Sun and Milliken, 2015; Pan et al., 2017). Compared to smectite, chlorite and serpentine (Ehlmann et al., 2010; Amador et al., 2018) are found in low and medium temperature metamorphic rocks that might exist at greater depths in the crust or linked to hydrothermal systems. Several studies are consistent with a relative increase in chlorite compared to smectite with depth (Carter et al., 2013; Sun and Milliken, 2015). Phyllosilicates have also been detected in Kalpin crater central peak north of the InSight landing site, excavated from 5 to 6 km depth, and in the transition unit south of the landing site (Pan et al., 2020); as these locations are more than 400 km away from InSight, this does not amount to a direct detection at the landing site, but it makes phyllosilicates a plausible option.

Sulfates are another type of hydrated minerals that have been observed in various locations on Mars, including around the equator (Ehlmann and Edwards, 2014). The Zhurong rover has recently identified hydrated sulfates or silica in southern Utopia Planitia, where they were previously not evident from orbit, indicating aqueous activity in the Amazonian (Liu et al., 2022).

Carbonates, another type of hydrated minerals, are rarely found at the present Martian surface, though Kissick et al. (2021) suggest that they could have commonly formed in crustal aquifers isolated from the Noachian atmosphere and have served as a sink for atmospheric carbon. Seismic velocities of calcite are similar to chlorite (Table 1), so we show no separate calculations here.

To investigate the influence of the possible range of hydrated minerals as cement and precipitates in cracks, we show results for two clay minerals that represent a broad range of elastic parameters, smectite and chlorite, as well as for the sulfate gypsum.

Table 1
Elastic parameters of rocks, minerals, liquids and gases used in the calculations.

Material	K [GPa]	μ [GPa]	ρ [kg/ m^3]	v_P [m/s]	v_S [m/s]	Reference
Basalt	74.0	38.1	2970	6482	3582	Woeber et al. (1963)
Plagioclase (Albite)	75.6	25.6	2630	6459	3120	Woeber et al. (1963)
Gabbro	94.0	49.0	2970	7325	4062	Iturrino et al. (1991)
Smectite	6.0	4.0	2290	2225	1322	Vanorio et al. (2003)
Gypsum	42.5	15.7	2317	5232	2603	Hearmon (1984)
Chlorite	64.9	30.4	2710	5930	3350	Katahara (1996)
Calcite	73.3	32.0	2712	6539	3435	Hearmon (1984)
Serpentine (Lizardite)	60.9	33.6	2516	6484	3657	Auzende et al. (2006)
CO_2 (20° C, 0.1 MPa)	0.0001	0	1.8	267	0	Lemmon et al., 2024
liquid H_2O	1.97	0	1000	1404	0	Wagner and Pruß (2002)
H_2O ice Ih (− 40° C)	8.25	3.58	922	3758	1971	Dantl (1968); IAPWS (2009)

3.4. Constraints on water saturation and ice

Pores and cracks might in addition be either filled by the Martian atmosphere or water, either in liquid form, potentially as brines, or ice. The Martian atmosphere consists of over 95 % CO_2, which, depending on temperature and pressure, could be gaseous, liquid or supercritical. Based on the low surface pressure of Mars (about 610 Pa) and a representative crustal temperature profile for the landing site (Supplementary Fig. S7) from thermal evolution models (Plesa et al., 2018, 2022), we calculated the isothermal density, bulk modulus and state of CO_2 at various crustal depths (Lemmon et al., 2024) and found that it remains a gas in all cases considered here.

Independent information on the possible existence of liquid water or ice in the crust is provided by 3D thermal evolution models, geology, orbital radar, and the scattering and attenuation of seismic waves. Thermal evolution models have been used to calculate the depth to the present-day ground-water table on Mars, in dependence on crustal thermal conductivity and the presence of salts in the water that could substantially lower freezing temperature (Plesa et al., 2020). We consider results from three different models here, spanning the range of average crustal densities compatible with Wieczorek et al. (2022) and the experimental range of thermal conductivities for basalt (Clauser and Huenges, 1995; Hofmeister, 1999), which lead to crustal thicknesses at the InSight landing site extending slightly beyond the limits given by Carrasco et al. (2023a) (see Supplementary Text S6.2 and Plesa et al., 2022, for details). For pure water, the resulting depth of the water table at the InSight landing site is between 2.1 km and 5.3 km for the different models, and, as temperature increases with depth, ice would be stable above, i.e. could potentially exist in layer 1 and a part of layer 2 (Supplementary Figs. S7, S8). Geologic and radar mapping of Elysium Planitia to the east of the landing site found that ice deposits near the surface were very likely in the past, and might still exist today in localized patches (Voigt et al., 2023).

A similar maximum extent of the cryosphere as at the landing site is expected along the great circle paths connecting InSight and S1222a (both minor and major arc, Fig. 1), as they extend close to the equator. The same is true for the S0976a piercing point locations and along the great circle arc connecting S1094b and InSight, which crosses Elysium Planitia. Water ice was excavated by the S1094b impactor (Posiolova et al., 2022), making the location of S1094b the lowest latitude on Mars where ice has directly been observed so far. The great circle path through InSight and S1000a extends further north, across an area where ice-exposing scarps have been identified in orbital photography (Dundas et al., 2021), and has on average a slightly, i.e. 1 to 2 km, larger water table depth than the landing site (Supplementary Fig. S8).

Dissolved salts up to an eutectic concentration of perchlorate would move the ground water table up to within less than 500 m of the surface at the InSight landing site, and at all other locations discussed above, according to thermal evolution models (Plesa et al., 2020, Supplementary Text S6.2). We considered various perchlorates, including $Ca(ClO_4)_2$, $Mg(ClO_4)_2$, and $NaClO_4$, which all have similar effects (Supplementary Fig. S8 and Text S6.2). Water saturation of layers 1 as well as the crust below is thus also consistent with these models, if salts, at a near-eutectic concentration in case of layer 1, are dissolved in the water.

Another observation speaks against the presence of liquid water over a substantial part of the crust, though: The modeling of high-frequency seismogram envelopes from InSight (Menina et al., 2021, 2023) requires a strongly diffusive, weakly attenuating layer that extends to at least 20 km depth in the vicinity of InSight and to 60 km depth along the ray path to event S1222a. The properties of this layer indicate that multiple scattering is the dominant seismic attenuation mechanism on Mars, and the contribution of absorption to attenuation is very small, which requires a heterogeneous and dry crust, excluding the presence of liquid water over a significant depth range like layer 2 or 3. Other independent studies obtained comparable results for scattering attenuation (Karakostas et al., 2021) and crustal attenuation in general (Garcia et al., 2022; Stähler et al., 2024). The study by Menina et al. (2023) also included other events besides S1222a at more than 600 km distance from SEIS, so the inferred dry crust is not just a local phenomenon at the landing site, but at least of regional scale. However, the crust is generally modeled as a single block in these studies (Menina et al., 2021, 2023; Stähler et al., 2024), and the effect of a 2 km thin layer below the seismometer in terms of scattering might not be substantial enough to be resolvable. Hence, saturation of layer 1 beneath the lander with liquid water in the form of brines is not excluded by these observations, but the presence of liquid water in pores or cracks over larger parts of the crust is not a relevant option at least for the InSight landing site and a broad region around it. Published constraints from attenuation were not considered by Wright et al. (2024) and Katayama and Akamatsu (2024) when modeling velocities in layer 3 by water-saturated rocks.

For our models, we study only the end-member scenarios of dry and fully water- or CO_2-saturated pores. Partial saturation might be present in the martian crust, but modeling such conditions would require an additional set of assumptions and parameters, which are unconstrained for modeling the micromechanics at the pore scale. The possibility of partial fluid saturation within the martian crust is only one of many parameters that can influence the assumptions and parameters in the Hertz-Mindlin theory. Grain contact forces are the backbone of such granular micromechanics theories, and the description and quantification of these forces would need to be adjusted for martian conditions as we gather more information in future missions. For example, the coordination number is an empirical parameter (Murphy III, 1982) measured on granular materials influenced by Earth's gravitational pull. Given that the gravitational pull on Mars is about one-third of that on Earth, what we know about grain contact force networks on Earth might differ under martian pressure, temperature, and fluid saturation conditions. Recently, Amos et al. (2024) used a heuristic modification of grain contact models to fit lunar seismic velocities, i.e. considering one-sixth of terrestrial gravity, in the uppermost 25 m, but also note that models based on Hertz-Mindlin theory provide accurate results for burial depths of several 100 m or more.

Details on the considered lithologies as well as the elastic parameters used are provided in Table 1 and Supplementary Text S6. Fig. 2 provides a schematic overview of the rock types, lithologies, and pore or crack fillings considered for each layer in our modeling.

4. Modeling results

In the following, we compare P- and S-wave velocity ranges and ranges of v_P/v_S ratios, which connect S- and P-wave velocities, from rock physics models as described above to the constraints from InSight. Here, the v_P/v_S ratio as independent, additional information is of special relevance to exclude some scenarios. However, this information is only available for the InSight landing site, which is, therefore, discussed in detail first.

Our rock physics models are compared to S- and P-wave velocity ranges from Carrasco et al. (2023b), P-wave velocity ranges in the uppermost 10 km of the crust from Kim et al. (2021), and ranges for v_P/v_S ratios from Joshi et al. (2023). We assume the later study is more accurate in terms of v_P/v_S ratios than Carrasco et al. (2023b) since it also includes multiple reflected and converted phases in the RFs, the timing of which have a well-known dependence on a layer's v_P/v_S ratio (Zandt and Ammon, 1995; Zhu and Kanamori, 2000). For the topmost 10 km,

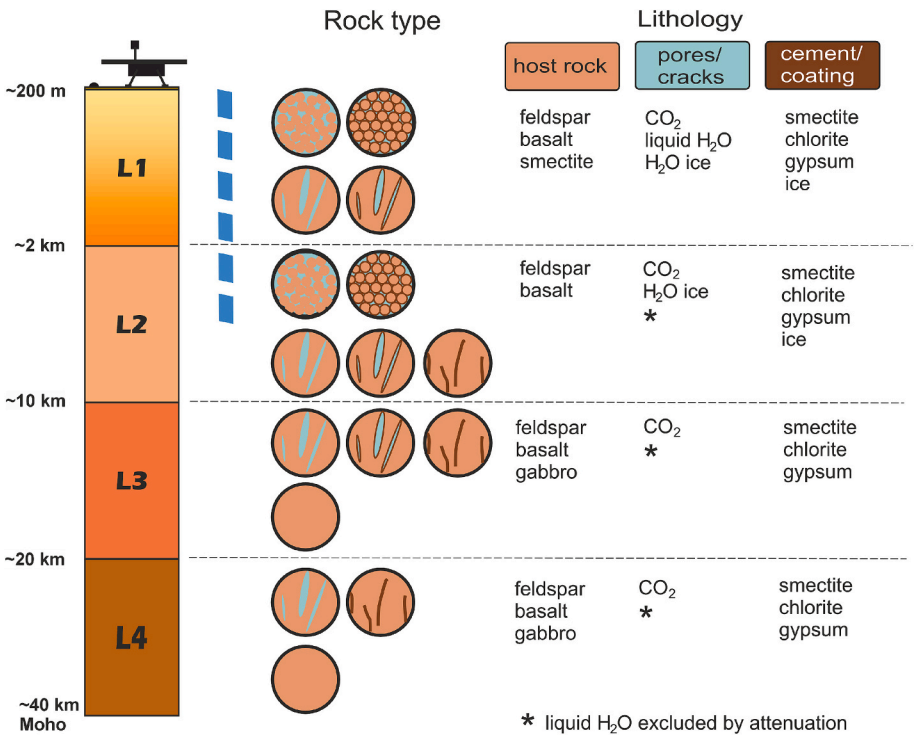

Fig. 2. Schematic overview of the rock types and lithologies studied in modeling the seismic constraints at the landing site. Layers 1 to 4 are labeled L1 to L4 here, and depth is not to scale. Vertical blue dashed line indicates range of water table depth at the landing site consistent with thermal evolution models. (For interpretation of the references to colour in this figure legend, the reader is referred to the web version of this article.)

there is a good agreement in the v_P/v_S ratio between the independent studies by Kim et al. (2021) and Joshi et al. (2023), and the values from Joshi et al. (2023) for all layers lie within the range of the models from Carrasco et al. (2023b), which did not use the additional information from later phases (e.g. Fig. 3i). Note also that the models from Carrasco et al. (2023b) are parameterized in terms of S- and P- wave velocities, while those from Joshi et al. (2023) are parameterized in terms of S-wave velocity and v_P/v_S ratio. Whereas a model might lie within both the independent ranges for S- and P-wave velocities, it might still be excluded by the link between permissible S- and P-wave velocities given by the v_P/v_S ratio.

The results from Carrasco et al. (2023b) are a representative selection of models that span the whole compatible parameter space, while the uncertainty in the other two studies is given in terms of the standard deviation σ. To ensure mutually compatible limits, we select a range of $\pm 2\sigma$ around the mean from these studies for comparison, which encompasses 95 % of all acceptable models in case of a Gaussian distribution. For locations away from the landing site, we compare with the velocity models as shown in Fig. 1.

4.1. Upper crust at the landing site

4.1.1. Sediments and sedimentary rocks

For dry, uncemented basaltic sediment, both P- and S-wave velocities are too low to fit the measured velocities in the uppermost two layers (Fig. 3a,e). The v_P/v_S ratio does not depend on the assumed critical porosity, but is significantly lower, outside the measured range, for rough as compared to smooth grain contacts. Considering a rock fully composed of feldspar compared to one with basaltic mineralogy changes velocities insignificantly, while assuming a clay composed of smectite instead results in even lower velocities (Supplementary Fig. S10).

Saturating the sediments with water increases P-wave velocities into the measured range, especially in layer 2, but has a negligible effect on the S-wave velocities (Fig. 3b,f). Accordingly, S-wave velocities are still outside of the measured range, and v_P/v_S ratios are rather high, above 2.0, at most considered depths for rough grain contacts, and even higher and outside the axis range for smooth grain contacts (Fig. 3j). The prominent increase in v_P/v_S ratio in saturated soils is consistent with terrestrial field observations (Pasquet et al., 2015).

Adding 2 % of cementation increases velocities to within the range of the InSight velocities, specifically in layer 1, regardless of the cementing agent (Supplementary Fig. S10), but results in too low v_P/v_S ratios for a dry rock, below 1.47, independent of where the cement is deposited with respect to the grains (Fig. 3c,g,k). These low v_P/v_S ratios are outside the range consistent with the InSight seismic data, even if we consider the estimates by Carrasco et al. (2023b) that provide independent v_P/v_S ratio estimates for layers 1 and 2 (light gray area in Fig. 3k), but have larger uncertainty in v_P/v_S as they did not explicitly consider multiple reflected phases. Increasing the amount of cementation, e.g. to 10 % or 20 %, provides a good fit to the P- and S-wave velocities in layer 2, but does not affect the low v_P/v_S ratios (Supplementary Fig. S11). We also considered a larger amount of cementation for gypsum and chlorite, which show a slightly different behaviors than smectite, but a simultaneous fit of S-wave velocities and v_P/v_S ratios in layer 1 or 2 is not possible. Therefore, dry cemented sedimentary rocks can be excluded in both layers 1 and 2.

Finally, saturating the cemented rock brings velocities and v_P/v_S ratio into the acceptable range for layers 1 and 2 (Fig. 3d,h,l), again independent of the choice of cement which could be smectite, chlorite, gypsum or ice. Saturation at this shallow depth is only compatible with

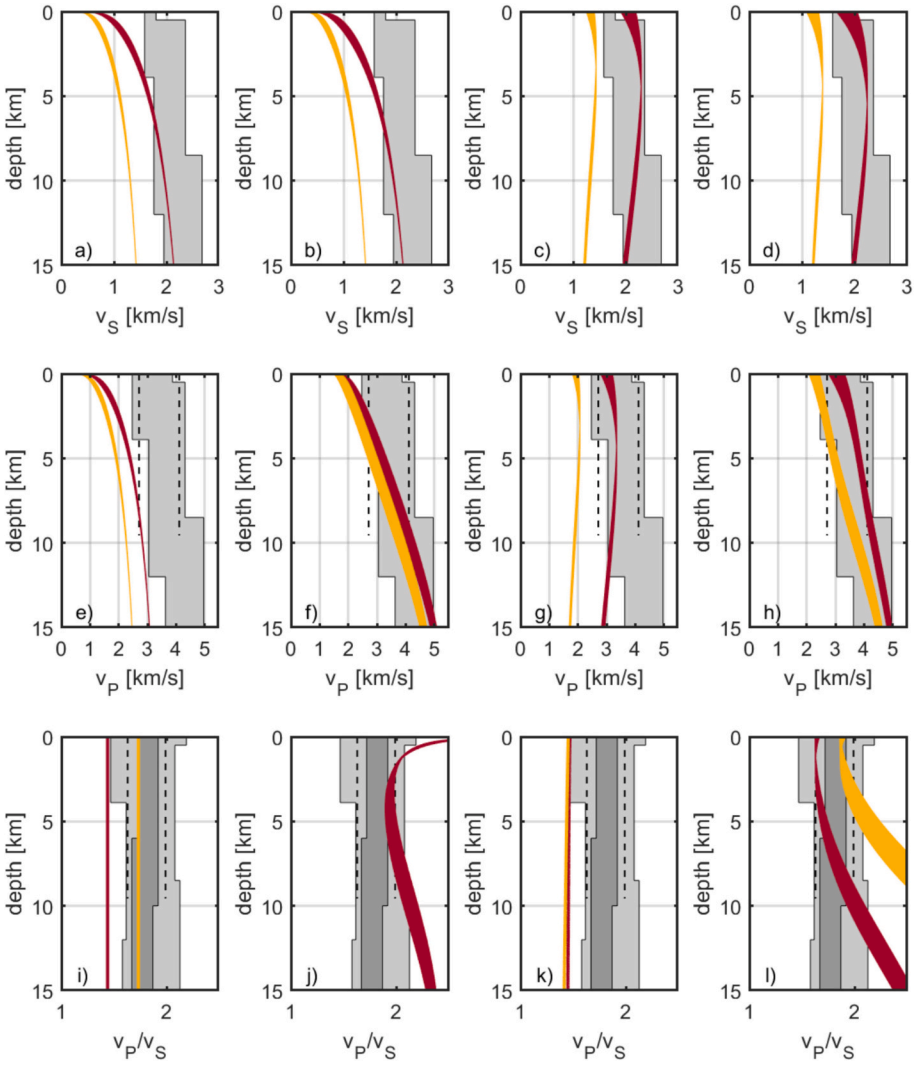

Fig. 3. Comparison of landing site velocity models by Carrasco et al. (2023b) (light gray shaded areas) and velocities predicted by modeling for unconsolidated and cemented basaltic sands. Dashed lines indicate P-wave velocity and v_P/v_S ratio within two standard deviations of the mean for the uppermost approximately 10 km from Kim et al. (2021), whereas medium gray outlines the v_P/v_S ratios within two standard deviations of the mean from Joshi et al. (2023). (a) S-wave velocities for dry basaltic sand with 100 % rough grain contacts (dark red) and 100 % smooth grain contacts (orange). The range of curves for each of the two cases results from varying surface porosity between 30 % and 50 %. (b) S-wave velocities for water-saturated basaltic sand. Colour coding as in (a). (c) S-wave velocities for dry basaltic sand with 2 % of pores cemented by smectite deposited either completely at grain contacts (dark red) or all around the grain surfaces (orange). (d) S-wave velocities for water-saturated basaltic sands with 2 % of smectite cementation. Colour coding is the same as in (c). (e-h) P-wave velocities, depicted as in (a-d). (i-l) v_P/v_S ratios, depicted as in (a-d). In cases (i) and (k), v_P/v_S ratios are independent of porosity. (For interpretation of the references to colour in this figure legend, the reader is referred to the web version of this article.)

brines, not pure water, according to thermal evolution models (Supplementary Text 6.2).

4.1.2. Cracked or porous rocks

When modeling cracked or vesicular rocks, we first consider a basalt rock, with a density compatible with zero-porosity basalt (Heap et al., 2020), to which cracks or pores are added. These cracks or pores are filled by the martian atmosphere, liquid water or ice, and modeling results compared with the P- and S-wave velocity ranges and ranges of v_P/v_S ratio in layer 1 for liquid water, and layers 1 and 2 for gas and ice, respectively (Fig. 4). As water saturation can be excluded a priori over extended ranges of the crust beneath InSight (see discussion in section 3.4), there is no need to examine water-filled cracks in layer 2.

In all considered cases, fitting P- or S-wave velocities is not possible with round pores, but requires elongated cracks (i.e. aspect ratios below 0.2). While dry fractured basalt, e.g. with porosities in the 10 to 20 % range, can explain the observed S-wave velocities (Fig. 4a), and a simultaneous fit to the observed P-wave velocity range is possible for layer 2 (Fig. 4d), these models have very low v_P/v_S ratios, below 1.5 for layer 1 and below 1.6 for layer 2 (Fig. 4g). Similar results are shown by Katayama and Akamatsu (2024), but their implications regarding layer 2 are not discussed in detail. Very low v_P/v_S ratios have been observed in the field for cracked rocks under low pressure (Flinchum et al., 2024), but they are not consistent with the InSight measurements of either the average v_P/v_S across layers 1 and 2 (Joshi et al., 2023; Kim et al., 2021) or the individual, more uncertain values for both layers (Carrasco et al., 2023b). Hence, these models can be excluded.

Completely filling all cracks or pores with ice results in too high S-wave velocities - porosities over 30 % are required to get into the velocity range of layer 2 (Fig. 4c), and more than 50 % would be necessary to obtain the low velocities in layer 1. As concluded by Manga and Wright (2021), a shallow cryosphere with 100 % ice saturation in cracks

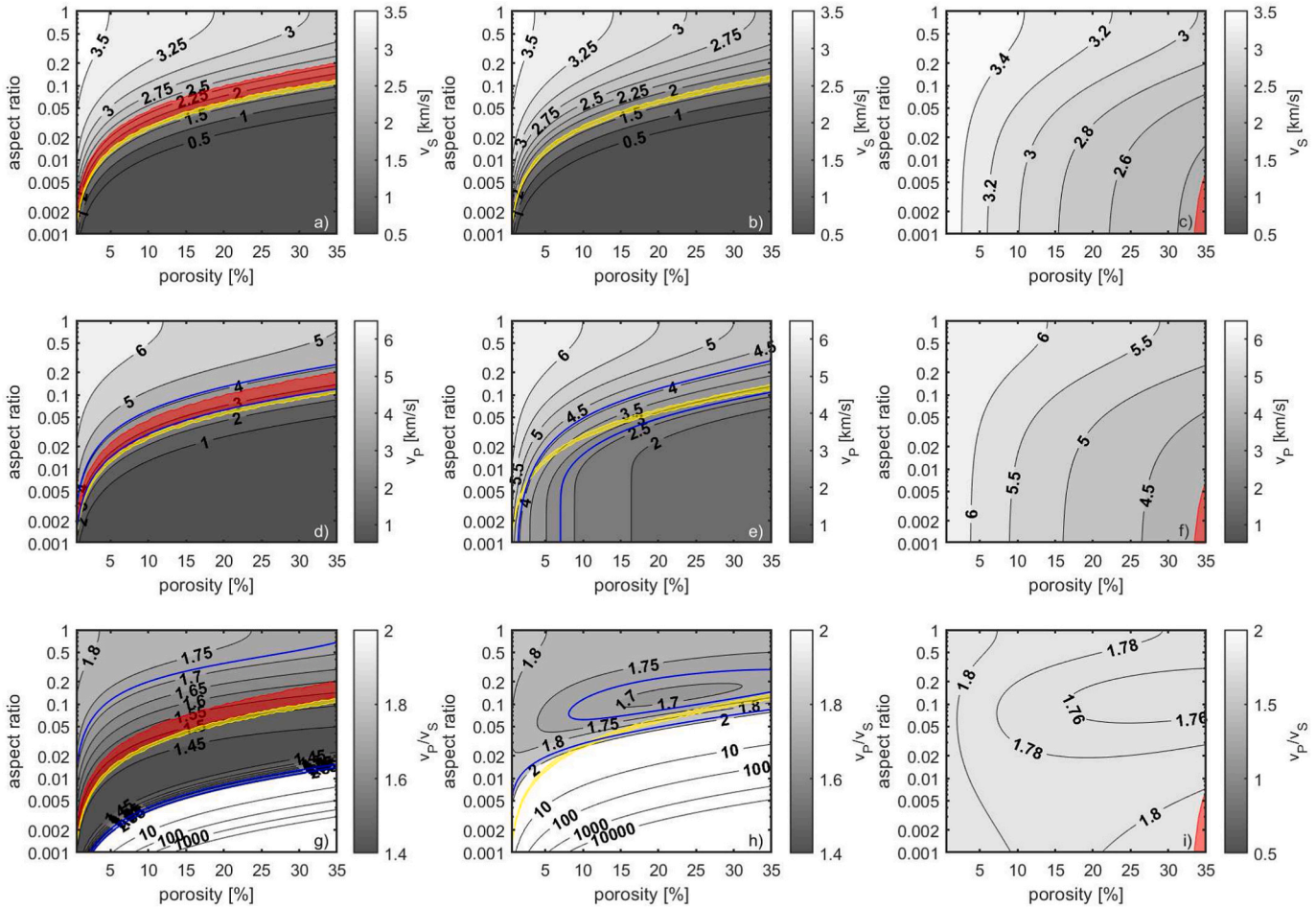

Fig. 4. S- and P-wave velocities and v_P/v_S ratios for fractured basaltic rocks with different crack filling at 100 % saturation. Graphs of S-wave velocity, P-wave velocity, and v_P/v_S ratio are shown in terms of porosity and crack aspect ratio. Columns represent the crack fill: CO2 gas, water, and ice from left to right. Rows from top to bottom are S-wave velocity, P-wave velocity, and v_P/v_S ratio corresponding to each of the crack fills. Colour overlays indicate the InSight model S-wave velocities, and associated porosity and aspect ratio combinations, in the top most (yellow) and second (red) layers at the landing site. Blue lines bound the areas of compatible P-wave velocities (Kim et al., 2021) in (d)-(f) and v_P/v_S ratios (Joshi et al., 2023) in (g)-(i) based on 2 σ ranges. The colored overlays are copied from (a)-(c) to (d)-(i) to indicate which parameter combinations, if any, can simultaneously fit constraints on S-wave velocities and P-wave velocities ((d)-(f)) or v_P/v_S ratios ((g)-(i)). (For interpretation of the references to colour in this figure legend, the reader is referred to the web version of this article.)

over kilometers of depth at the landing site can accordingly be excluded.

On the other hand, water-filled pores or cracks provide S- and P-wave velocities and v_P/v_S ratios within the observed range for porosities between 11 % and up to 35 % and aspect ratios between 0.032 and 0.135 for layer 1 (Fig. 4b,e,h), where the lower porosity bound is given by the constraint on v_P/v_S. When considering a more felsic rock instead of basalt, the general conclusions remain the same (Supplementary Fig. S12).

Considering a cracked or vesicular basalt with some amount of coating within the cracks or pores, filling as little as 5–10 % of the cracks with alteration products already has a distinct influence on S-wave velocities as well as v_P/v_S ratios (Fig. 5). We only discuss the combined constraints from S-wave velocities and v_P/v_S ratios in the following since P-wave velocities offer very limited additional information (Supplementary Figs. S13 and S14).

Generally, a higher initial porosity is required to match the S-wave velocities compared to results without any coating (Fig. 4). Similar to the case with no coating, no amount of porosity and pore filling results in compatible S-wave velocities for aspect ratios above 0.2, i.e. vesicular basalts with rounded pores again cannot explain the data. For a coating of smectite, the mineral with the lowest elastic moduli considered (Table 1), the S-wave velocities in the first and second layer can be explained with less than 5 % porosity for very elongated cracks, with aspect ratios below 0.01 (Fig. 5a). However, the v_P/v_S ratios corresponding to the measured S-wave velocities still remain too low, below 1.7, regardless of the amount of coating, in case of gas-filled cracks (Fig. 5a), so this scenario can be excluded when comparing to the average v_P/v_S ratios of layers 1 and 2 (Kim et al., 2021; Joshi et al., 2023). Note, though, that a lower v_P/v_S ratio in layer 2, within the modeled range, could in this case potentially be compensated by a higher v_P/v_S ratio above 2.0 in layer 1 when using the independent, less well-constrained ranges for both layers (Carrasco et al., 2023b). In case of water-filled cracks, v_P/v_S ratios increase to cover a range between 1.68 and 4.0, dependent on the amount of coating. Porosities of for example 20 % in layer 1, with 20 % coating by smectite and the remaining part of the crack filled with water, could fit S-wave velocities, v_P/v_S ratios and P-wave velocities (Supplementary Fig. S13) for a crack aspect ratio of 0.03 (Fig. 5b).

For other types of coating, such as ice, sulfate or chlorite, 5–10 % of coating brings v_P/v_S ratios in the range observed by InSight for gas-filled cracks in both layers 1 and 2, especially for low aspect ratios (Fig. 5c,e,g). More than about 20 % and 10 % of coating in layer 1 can be excluded in case of gypsum and chlorite, respectively, as this would require an initial porosity above 40 % (Fig. 5d,e). Filling the cracks with water

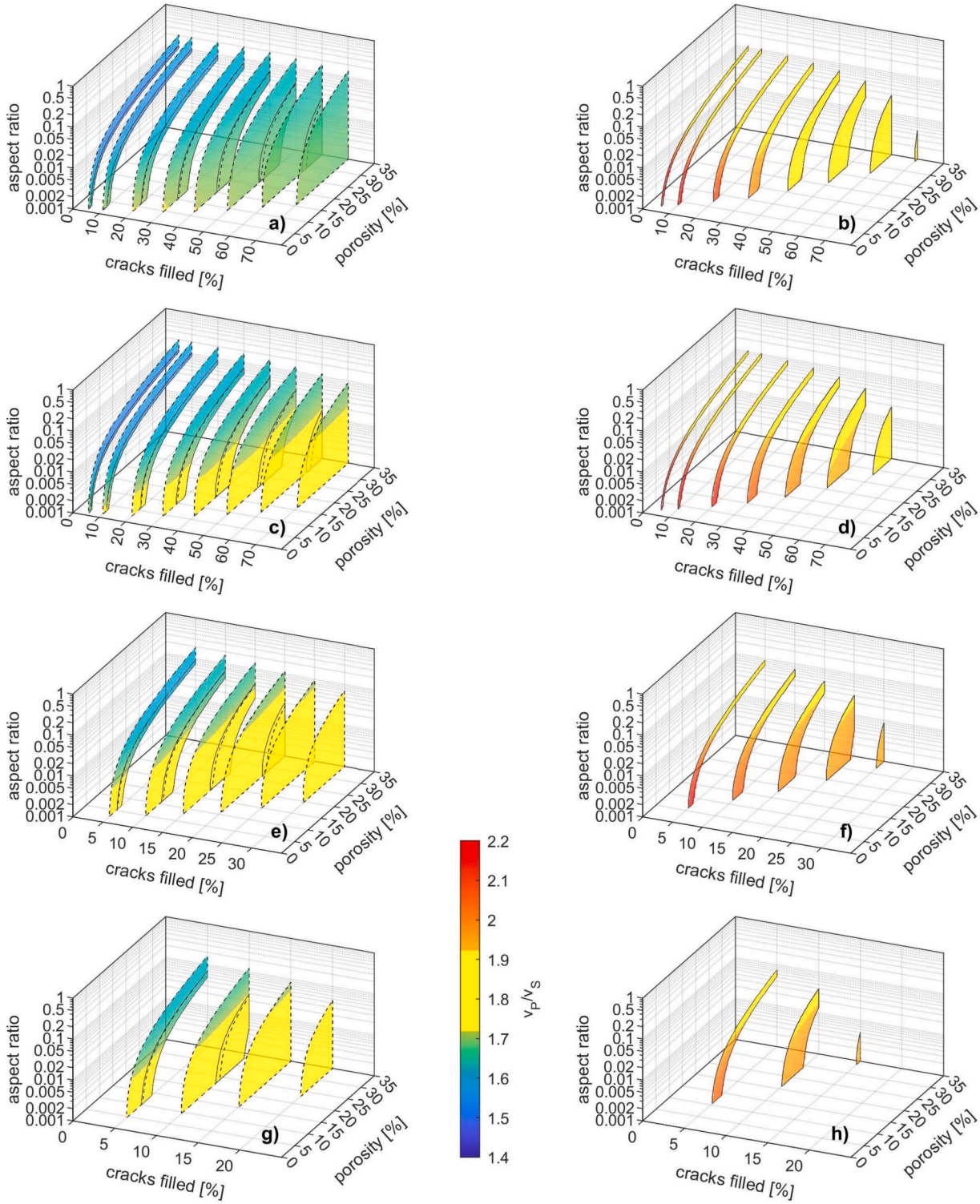

Fig. 5. Variation of S-wave velocities and v_P/v_S ratios for cracked basaltic rock with partly cemented cracks against crack aspect ratio, amount of crack filling, and porosity. For each amount of crack filling, the colored areas outline the region where S-wave velocities agree with layer 1 (solid gray outline) or layer 2 (dashed black outline), respectively. Areas that do not agree with those S-wave velocities are left blank. Colour coding refers to v_P/v_S ratio as indicated, with yellow marking values within the two sigma range derived by Joshi et al. (2023). Plots on the left are for CO_2 in the cracks, whereas those on the right are for H_2O. (a,b) Clay coating. (c,d) Ice coating. (e,f) Gypsum coating. (g,h) Chlorite coating. (For interpretation of the references to colour in this figure legend, the reader is referred to the web version of this article.)

instead of gas increases the v_P/v_S ratios and shifts the acceptable parameter range to lower aspect ratios and higher initial porosities (Fig. 5 d,f,h).

Considering a felsic rock instead of basalt, compatible S- and P-wave velocities and v_P/v_S ratios can be found for all types of coating considered, including smectite, whereas more than about 20 % and 10 % of coating in layer 1 can again be excluded in case of gypsum and chlorite (Fig. 6). Additionally, the seismic constraints can be fit by a felsic rock

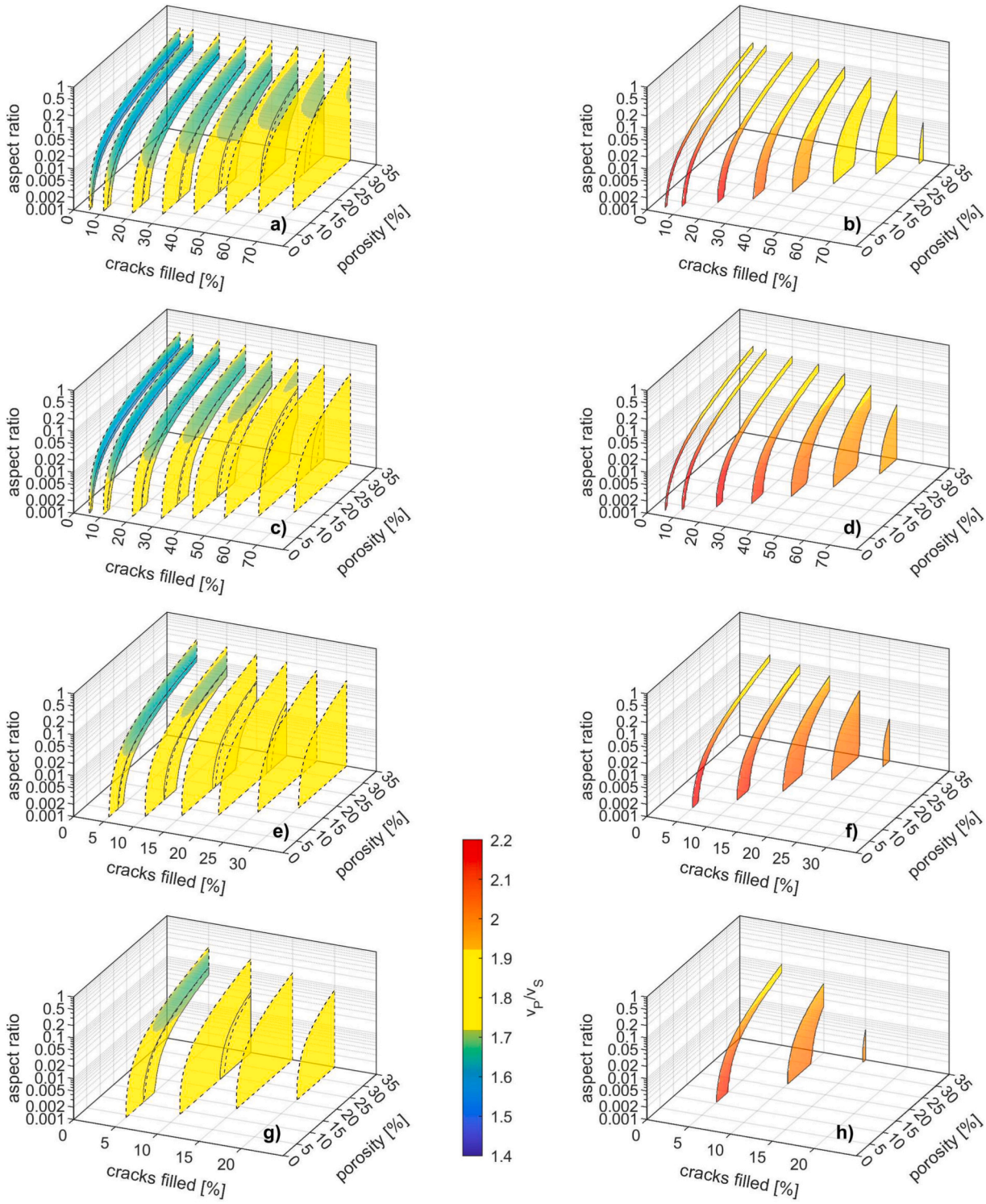

Fig. 6. Same as Fig. 5 for a cracked felsic rock (plagioclase).

with more than 23 % porosity if 100 % of the cracks are sealed by smectite, i.e. the rock is permeated by smectite veins. The effect of water saturation is comparable to the case for basalt.

4.1.3. Possible scenarios

In summary, there are four scenarios that are compatible with the InSight data for layer 1 (Table 2): Either water-saturated cemented sediments (e.g. basaltic sand with 2 % smectite cementation), or dry, gas-filled cracked rocks with some amount of coating (e.g. basalt with 22 % porosity and cracks filled with 40 % ice or cracks filled with 15 % gypsum, or feldspar with 20 % porosity and cracks filled with 40 % smectite), or water-saturated cracked rocks with or without coating. For layer 2, on the other hand, since water saturation can be excluded based on scattering and intrinsic attenuation (Menina et al., 2023; Stähler et al., 2024), there is only one compatible scenario, which is dry cracked rocks with some coating, such as basalt with 18 % porosity and cracks filled with 50 % ice, or 20 % gypsum, or 10 % chlorite, or feldspar with 18 % porosity and 50 % smectite or ice, or 20 % gypsum, or 10 %

chlorite filling the cracks, up to the extreme case of 100 % of cracks filled by smectite in a felsic rock with more than 23 % cracks. Only the combination of basalt with smectite can be excluded.

These exemplary combinations of porosity and coating would result in a net amount of less than 10 % clay or sulfate in the host rock, though larger amounts are possible when combined with higher initial porosities, and especially for the case of a felsic rock with smectite veins and no remaining porosity. Subsurface amounts of less than 10 % of hydrated minerals would be well in keeping with orbital estimates (Riu et al., 2022; Wernicke and Jakosky, 2021), which found average abundances of individual hydrated minerals per detection of 3 % to 14 % and typical overall abundance between 5 % and 20 %. These estimates might be biased, though: lower overall abundances of less than 5 % of hydrated minerals might not be detectable from orbit, sulfates were excluded from these studies, and the spatial footprint of the orbital data ranges from hundreds of meters to several kilometers, i.e. integrates over many

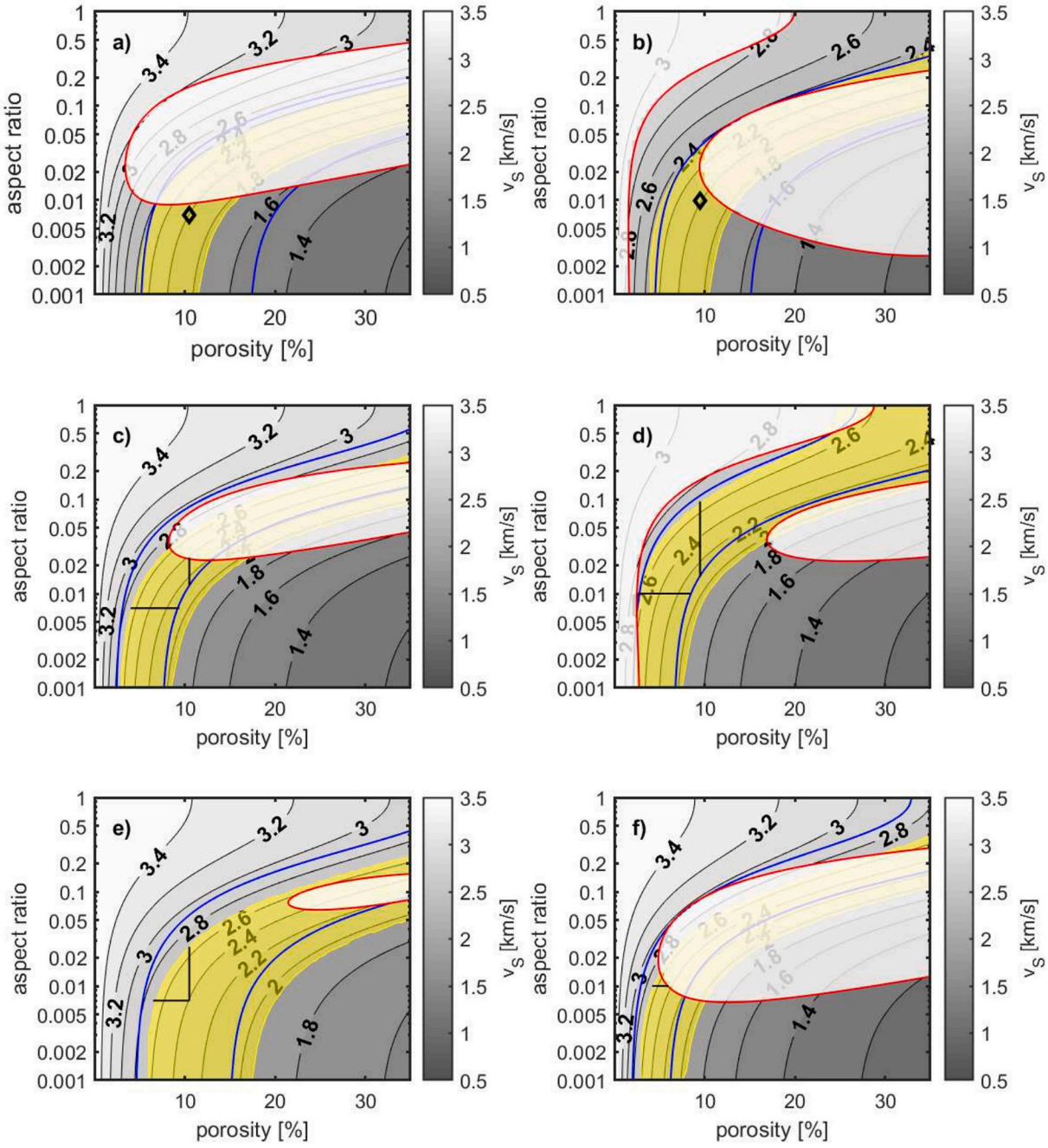

Fig. 7. Permissible parameter range in terms of porosity and aspect ratio for different depth ranges beneath InSight and different compositions. (a) Cracked basalt with CO_2 in the cracks and 10 % of the voids coated by gypsum. Contour plot is for S-wave velocities in layer 2, where the yellow area indicates S-wave velocities in agreement with InSight models. Blue lines outline the area compatible with P-wave velocities from InSight, whereas the white region with red boundary is excluded based on v_P/v_S constraints from InSight. Black diamond marks a possible parameter combination for an S-wave velocity of 2 km/s. (b) Same as (a), but for cracked felsic rock with 30 % of the voids coated by smectite. (c) Same composition as in (a), but with constraints for layer 3. Black horizontal and vertical lines, together with the other constraints, mark parameter space consistent with a velocity increase compared to layer 2. (d) Same as (c), but for composition in (b). (e) Alternative option to explain larger velocities in layer 3 than in 2 by changing the crack coating from (a) to 10 % chlorite. (f) Alternative option to explain larger velocities in layer 3 than in 2 by changing the rock matrix from plagioclase in (b) to basalt, likewise with 30 % smectite coating. (For interpretation of the references to colour in this figure legend, the reader is referred to the web version of this article.)

of the coated cracks within our rock-physical models.

To explain the observed azimuthal anisotropy (Li et al., 2022b), we only consider cracks filled with CO_2 and some coating, as derived above for layer 2, since fluid-filled cracks can be excluded and gas-filled cracks with coating are already required to decrease velocities into the observed range. It is thus more likely that some of these cracks have a preferred orientation than that additional faster inclusions exist. Indeed, for the two exemplary cases shown in Fig. 7 a), b), an additional porosity of 1–3.5 % of east-west aligned cracks, with the same aspect ratio and amount of pore filling, is sufficient to explain the anisotropy as well as fit SV- and P-wave velocities (Supplementary Fig. S15). Due to the trade-offs between aspect ratio and amount of pores, a similar effect on velocities could also be attributed to either a higher amount of additional aligned porosity with higher aspect ratios, or a lower amount of additional aligned porosity with lower aspect ratios (e.g., Fig. 7d of Li et al., 2022b). Since we are only considering two exemplary cases here, though, we chose to assume the same aspect ratio for both randomly oriented and aligned cracks.

4.2. Middle and lower crust at the landing site

We do not consider sediments or sedimentary rocks in the deeper crust, as sediments are expected to be confined to shallower depth on Mars (e.g. Fig. 1b in Wilson and Head III, 1994). In fact, for large amounts of cementation, the P- and S-wave velocities of layer 3 could be fit with a model of basaltic sediment, but the v_P/v_S ratio remains below the range derived from seismic data (Supplementary Fig. S11, Table 2).

When the velocities in layer 2 are modeled by dry cracked rocks with some amount of coating, there are several ways to explain the increase in velocities in layer 3. It is important to highlight that our modeling

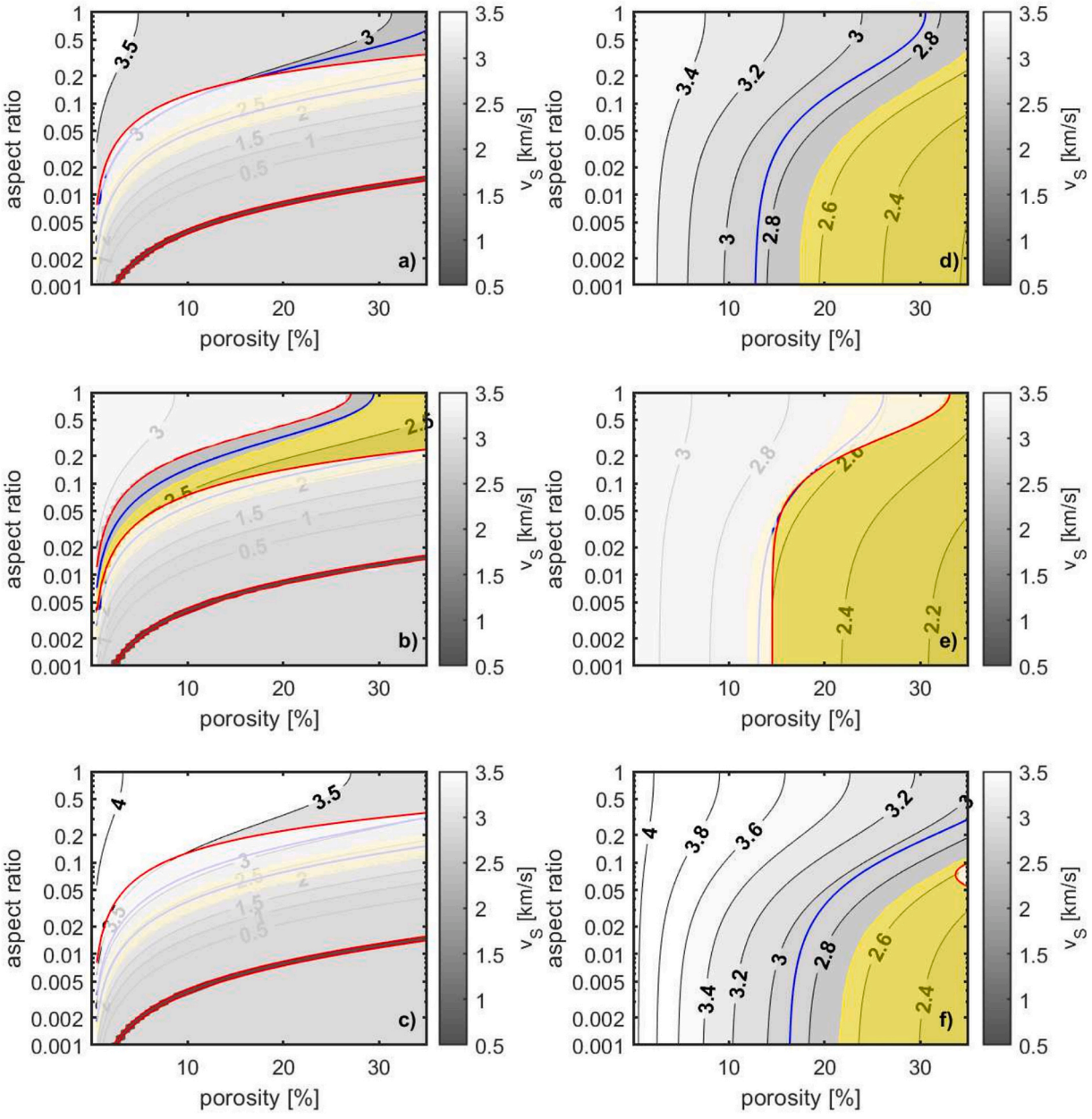

Fig. 8. S-wave velocities versus aspect ratio and porosity (contour plot) for different rock types for cracked rock with CO_2 pore-filling (left), and smectite pore filling (right), compared to constraints for layer 3 beneath InSight. Yellow area is permissible in terms of S-wave velocities, whereas blue lines outline area consistent with P-wave velocities and white regions with red boundary mark areas excluded based on v_P/v_S ratio. (a,d) Basalt (b,e) Feldspar (c,f) Gabbro. (For interpretation of the references to colour in this figure legend, the reader is referred to the web version of this article.)

provides different combinations of porosity and aspect ratios that fit the InSight constraints equally well. Next we discuss two examples of porosity-aspect ratio combinations for layer 2, assuming an S-wave velocity of 2 km/s in that layer (Fig. 7). The actual range of permissible S-wave velocities is 1.76 km/s to 2.36 km/s (Carrasco et al., 2023b). The examples are cracked basalt with 10.5 % gas-filled porosity, with 10 % of the cracks with an aspect ratio of 0.007 filled with gypsum (Fig. 7a), and cracked felsic rock with 9.5 % gas-filled porosity, with 30 % of the cracks with an aspect ratio of 0.01 filled with smectite (Fig. 7b).

With the same amount of pore filling, a higher velocity can be obtained by a lower initial porosity or a higher aspect ratio, or a combination of both (Fig. 7c,d). Impact-generated porosity is expected to decrease with depth as large impacts, that are basin-forming for example, and affected the entire crustal structure (Branco et al., 2024), were exclusive during heavy bombardment within the first billion years since planet formation (Werner, 2014, 2019). Subsequent smaller impacts only affected shallower crustal layers (Melosh, 2011), so the destruction and generation of additional porosity by these impacts (Wahl et al., 2020) would be limited to shallower depths. In addition, both elastic and viscous pore closure will become more important with depth and inevitably close the fracture and pore space created by impacts and other processes (Wilson and Head III, 1994; Gyalay et al.,

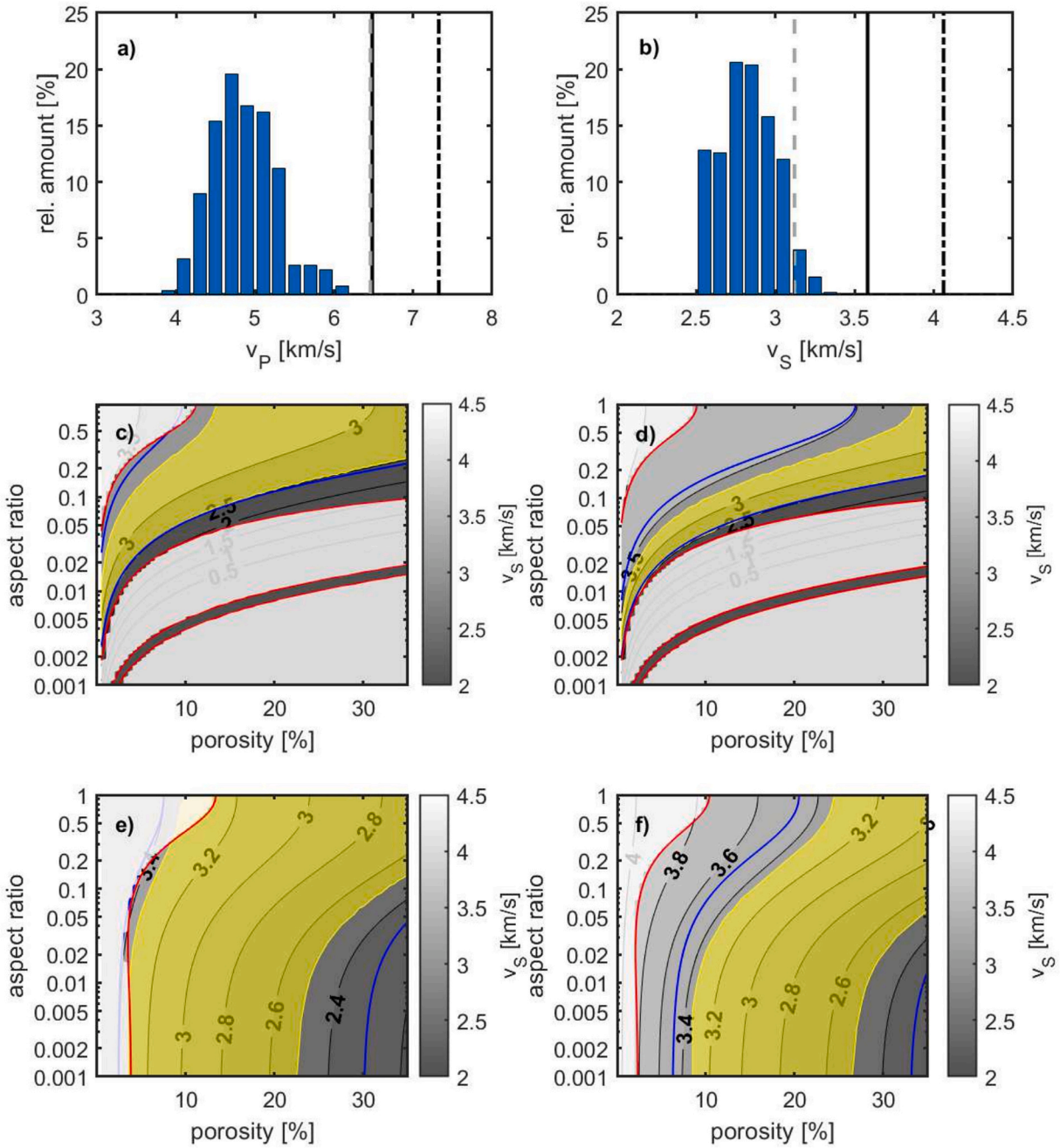

Fig. 9. (a) P-wave velocity range beneath InSight in layer 4, compared to velocities of plagioclase (gray dashed line), basalt (black solid line) and gabbro (black dash-dot line), based on Table 1. (b) Same as (a) for S-wave velocities. (c) S-wave velocities against porosity and aspect ratio (contour plot) for cracked basalt with CO_2 in the cracks against constraints in layer 4 beneath InSight. Yellow area is permissible in terms of S-wave velocities, whereas blue lines outline area consistent with P-wave velocities and white regions with red boundary mark areas excluded based on v_P/v_S ratio. (d) Same as (c) for cracked gabbro. (e) Same as (c) for cracked basalt with smectite filling all fractures completely. (f) Same as (e) for cracked gabbro. (For interpretation of the references to colour in this figure legend, the reader is referred to the web version of this article.)

2020). Cracks with the lowest aspect ratios are the first to be sealed or closed under pressure (Wilkens et al., 1991; Walsh, 1965), resulting in an increase in aspect ratio with depth (Supplementary Fig. S9).

Another way to increase velocities in layer 3 compared to layer 2 while keeping porosity and crack aspect ratio constant would be to increase the amount of crack coating with a thicker alteration layer within the cracks at depth. As we assume that a coating by hydrated minerals is caused by aqueous alteration, a thicker alteration layer with depth would require enhanced interaction with water at depth, suggested by Manga and Wright (2021) as the result of an ancient crustal aquifer. Crustal hydration through irreversible chemical weathering is considered an important mechanism for water loss on early Mars, including a substantial amount of crustal hydration in the Noachian from a reservoir in the upper crust, with subsequent reduced hydration in the Hesperian, and negligible crustal hydration in the Amazonian (Scheller et al., 2021). At the depth range considered here, the crust at the landing site is Noachian and would have experienced hydration from the top down according to this model. Hence, we do not consider a thicker alteration layer at depths below 10 km likely, though it would be compatible with the seismic data. If, on the other hand, a decrease in alteration with depth is considered, it would also be possible to meet all constraints for layer 3, but a further decrease in initial porosity and/or increase in aspect ratio would be required (Fig. 5e), which might conflict with the constraints on the v_P/v_S ratio in case of feldspar.

Explaining the P- and S-wave velocities and the v_P/v_S ratio in layer 3 is actually possible for a porous rock fully composed of feldspar with CO_2 pore filling and no alterations (Fig. 8b) for a wide range of porosities and aspect ratios, e.g. for 10 % porosity and an aspect ratio of 0.09. This is not the case for basalt and gabbro, where it is impossible to simultaneously satisfy the constraints on S-wave velocity and v_P/v_S ratio for a cracked rock without any alteration (Fig. 8a, c). In addition, the seismic constraints can also be met by a basaltic, felsic or mafic rock with porosities above 19 %, 15 % and 23 %, respectively, and all cracks filled to 100 % with smectite (Fig. 8d)-f)). Other hydrated minerals, i.e. gypsum or chlorite, result in too high velocities and can be excluded.

Finally, the increase in velocities from layer 2 to layer 3 could also coincide with a change in composition. For example, the hydrated mineral at larger depth could be chlorite instead of gypsum, forming under higher temperatures deeper in the crust (Fig. 7e). Or near-surface felsic rocks could be replaced by basalt at larger depth, with the same mineral coating the cracks and a somewhat reduced porosity (Fig. 7f).

Velocities in the lower crust, given by layer 4 beneath InSight, are still too low for intact basalt or gabbro, and specifically the P-wave velocities are also too low for intact felsic rock (Fig. 9a,b). However, as little as 1 % dry porosity without any alteration and an aspect ratio of 0.02, which is possible at the considered depths for low porosities (Supplementary Fig. S9), would be sufficient to explain the velocities and v_P/v_S ratio in this layer for both basalt and gabbro (Fig. 9c,d). In shallower layers, the measured v_P/v_S ratio is higher (Joshi et al., 2023) and could thus not be fit for dry basalt or gabbro without any alteration (Fig. 8 a,c).

Alternatively, any previous cracking or fractures might have closed below 20 km depth, but their outlines might still persist in the form of veins resulting from hydrous alteration. Specifically, as little as 5 % of smectite-filled cracks in the case of basalt, or 12.5 % of smectite-filled cracks in the case of gabbro, might fit the observed constraints (Fig. 9e,f). For other alteration products like gypsum, chloride, or calcite, the volume of veins required to fit P- and S-wave velocities would be significantly larger (e.g. 23 % for basalt and 45 % for gabbro in case of gypsum), and v_P/v_S ratios could not be fit at all.

The models that are consistent with the seismic constraints are summarized in Fig. 10, which also indicates the preferred model based on the discussion in section 5.

4.3. *The crust away from the landing site*

4.3.1. *S0976a bounce point*

All rock physics models for layers 1 to 3 at the landing site could also explain the data at the bounce point, but the dispersion data especially from S1222a and the differential travel-time from S0981c make it

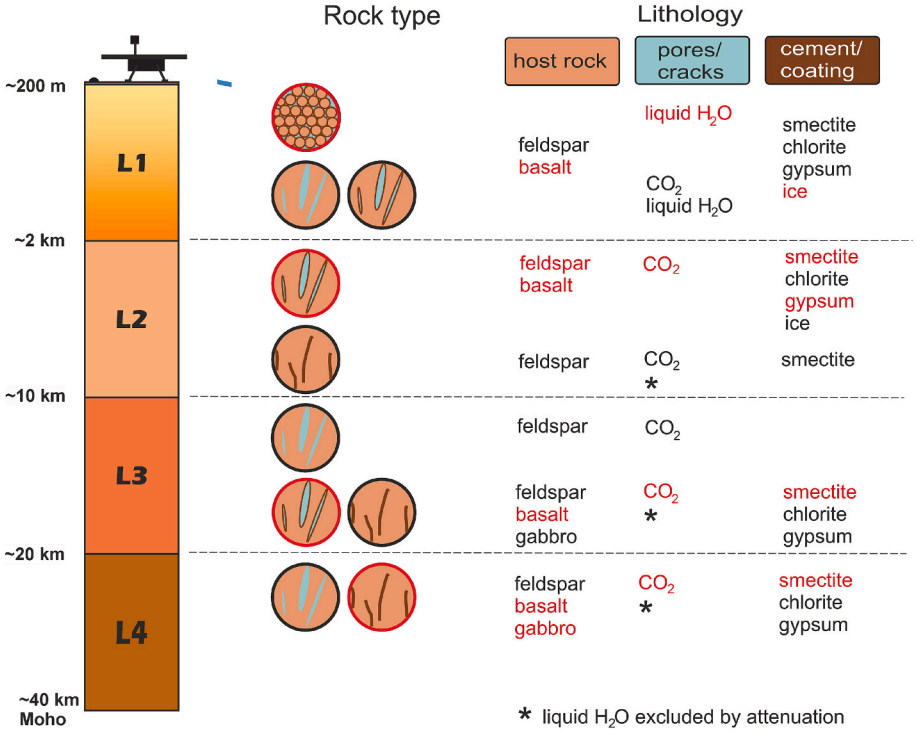

Fig. 10. Schematic overview of the rock types and lithologies consistent with the seismic constraints at the landing site, i.e. down-selected from options shown in Fig. 2. The preferred model is indicated by red edging and red letters. To allow for liquid water in L1, the water table would in this case be located near the surface (blue mark). (For interpretation of the references to colour in this figure legend, the reader is referred to the web version of this article.)

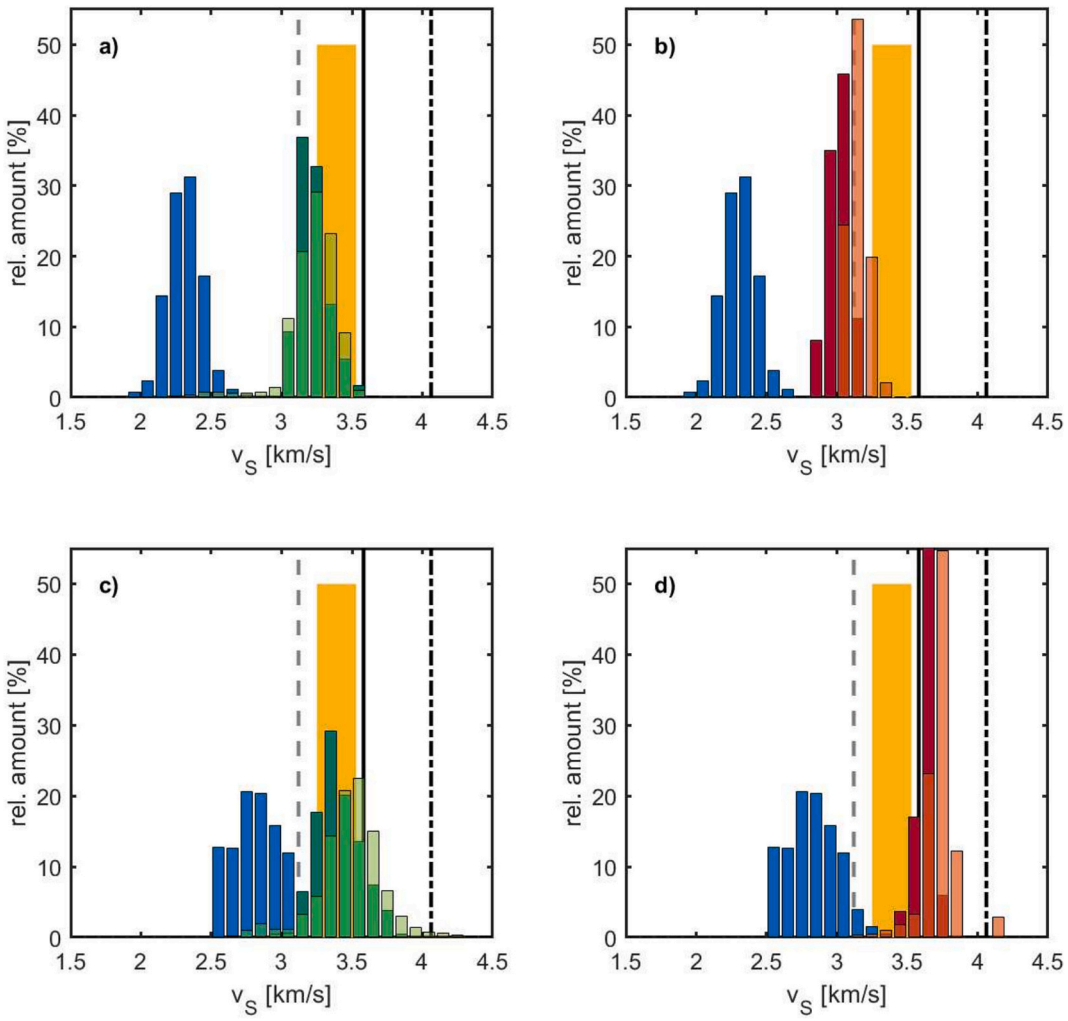

Fig. 11. Comparison of S-wave velocity constraints at different depth levels from landing site models and surface wave models over larger areas of Mars. In each subplot, vertical lines outline velocities of rocks based on Table 1, with plagioclase indicated by the gray dashed line, basalt by the black solid line and gabbro by the black dash-dot line. Orange bar in each subplot indicates the average crustal velocities from multi-orbit Rayleigh waves along the S1222a great circle path (Kim et al., 2023a). Blue histogram in each case refers to the velocity model for the landing site (Carrasco et al., 2023b). (a) S-wave velocities in the middle crust for layer 3 beneath InSight (blue), compared to depth range of 5 to 20 km for models based on Rayleigh wave dispersion from S1094b (dark green) and 12 to 20 km for models based on Rayleigh wave dispersion from S1000a (light green, Kim et al., 2022). (b) Same as (a) compared to velocities between 10 and 25 km along the minor arc between InSight and S1222a, based on Xu et al. (2023) (dark red) and Kim et al. (2023b) (light red). (c) Same as (a) for layer 4 beneath InSight and the depth range of 25 to 30 km and 25 to 40 km for the surface wave models, respectively. (d) Same as (b) for layer 4 beneath InSight and the depth range of 40 to 60 km for the surface wave models. (For interpretation of the references to colour in this figure legend, the reader is referred to the web version of this article.)

unlikely that these models apply to a continuous region between InSight and the bounce point location. Rather, they appear relevant only locally for these two locations.

We also examined the possible influence of anisotropy, since the analysis of the crustal reflections at the bounce point uses SH-waves, whereas the RF models for the landing site are based on SV-waves. However, we consider this explanation for the low velocities at the bounce point unlikely (see discussion in Supplementary Text S7).

4.3.2. Models along surface wave great circle paths

The models derived from surface waves have limited vertical resolution compared to the landing site models and are also less apt at resolving discontinuous changes in velocity. Specifically, none of these models can resolve the velocities of the uppermost 5 km of the crust (Fig. 1), so they cannot address the question of a global impact-generated high-porosity layer near the surface or provide information on the vertical and horizontal extent of ice exposed by impacts or along scarps (Dundas et al., 2021, 2023). Additionally, surface waves mainly constrain S-wave velocities, so no information on P-wave velocities or v_P/v_S ratios is obtained from these data. Since the models, especially the ones for S1222a (Fig. 1e), have nearly constant velocities over certain depth ranges and show stronger gradients in-between, Fig. 11 compares the S-wave velocities within these depth ranges to the corresponding values at the landing site.

Compared to layer 3, S-wave velocities above 20 km depth for great circle paths to the north-east of InSight (Fig. 11a) and between 10 and 25 km depth along the great circle path to S1222a (Fig. 11b) are distinctly higher and show overlap with the velocity of pristine plagioclase, but are lower than the S-velocities of pristine basalt or gabbro. In addition to intact felsic material, the measured velocities can be explained by cracked basalt or gabbro, with or without alterations. Since only S-wave velocities are available, porosities between 1 and 30 % remain possible for intact as well as altered basalt or gabbro (Fig. 8a,c, Fig. 7c), and no limits on the crack aspect ratio can be derived other than those based on crack closure with depth (Supplementary Fig. S9).

Considering layer 4 and shear wave velocities in the lower-most part of the crust resolved in the individual models, velocities at the landing site are still lower than elsewhere on Mars. In contrast to the landing site

models, all surface wave-derived S-wave velocities are consistent with intact basalt and approach the value for gabbro (Fig. 11c,d).

SV-velocities derived from S1222a for a model with anisotropy combined with a monotonous increase in velocity with depth on the one hand (Kim et al., 2023b), and a model with alternating high and low velocity layers that cause apparent anisotropy on the other hand (Xu et al., 2023) show good agreement in the considered depth ranges. However, between those ranges, the layered model contains significantly higher velocities consistent with intact basalt or gabbro between 3 and 10 km depth, and between 25 and 40 km depth. This alternating velocity structure is neither required nor consistent with the RF data from the landing site, at least if the layers are on a 10-km scale that would be well resolvable by RFs. Since Love waves were only observed for the minor-arc propagation from S1222a, complimentary information on differences between Love and Rayleigh wave velocities along great circle paths covering other regions of Mars are missing.

5. Discussion

Wieczorek et al. (2022) provide various scenarios to explain the crustal layering at the InSight landing site. Since we want to discuss these scenarios in the light of our modeling results, we briefly list their main points here. Low velocities down to about 10 km depth could either be explained by layered sedimentary deposits, or by extrusive lavas that are highly fractured and/or affected by substantial aqueous alteration. The velocity increase at 10 km depth beneath the landing site could be attributed to a reduction in porosity due to increased precipitation of minerals in an ancient aquifer (Manga and Wright, 2021), whereas the increase at 20 km depth could be caused by viscous pore closure (Gyalay et al., 2020). Both the upper or middle crustal layer could however also be related to the up to 11 km thick ejecta blanket from the Utopia impact, or been caused by changes in rock crystallinity, i.e. from sedimentary to fine grained to coarse grained rocks, comparable to the layering of oceanic crust on Earth. Layering could also be caused by compositional differences due to impact melt differentiation after the proposed Borealis impact.

The shallow part of the crust, to about 5 km depth, is only reasonably well resolved by the seismic data beneath InSight. The surface wave models for other regions of Mars show a tendency towards reduced S-wave velocities between 2 and 3 km/s above 5 km depth that could be similar to layer 2 at the landing site, but any detailed discussion is prevented by their limited resolution at shallow depth. For locations closer to centers of magmatic activity, e.g. Tharsis or Elysium Planitia (Voigt et al., 2023; Broquet and Andrews-Hanna, 2023), a thicker veneer of Hesperian and Amazonian lava flows than at the landing site, where they only cover the uppermost approximately 170 m (Warner et al., 2022), is expected. However, there are no seismic constraints on how regional geology might affect layering in the upper crust at these locations. Hence, layers 1 and 2 at the landing site are first discussed separately.

5.1. Upper crust at the landing site

5.1.1. Evidence for sediments in layer 1

Both sediments or cracked basalt in layer 1 can explain the observed seismic velocities (Table 2). Information from geology strongly supports sediments: Based on the absence of rocky ejecta craters with diameters larger than 2 km, it was concluded that the rocky unit (Amazonian-Hesperian lava flows) beneath the InSight landing ellipse extends no deeper than about 170 m, and a finer-grained, possibly sedimentary, layer without boulder-sized rocks lies below (Golombek et al., 2017; Warner et al., 2022). Orbital images also show that large, fresh impact craters with diameters larger than 10 km near the smooth plains of the InSight landing site lack rocks in their ejecta (Golombek et al., 2017, 2018). Since cratering mechanics suggests that the ejecta for craters with 10 km diameter can be excavated from up to 1 km depth, this

Table 2
Simplified summary of results in terms of lithologies consistent with seismic velocity constraints for the individual layers (abbreviated as L1 to L4) of the landing site model. Red cells marked with an "X" indicate lithologies excluded because they cannot reproduce the seismic constraints. Gray cells are excluded because they are not consistent with other constraints, e.g. based on attenuation or geology. Results for gray cells with a mark are included in the calculation and shown in figures. Green cells with a check mark are consistent with the constraints, and those marked in dark green indicate the preferred model. See text for details. By wet, we refer to water-saturated sediments and rocks. For sedimentary rocks, the type of cement cannot be distinguished (see Supplementary Fig. S10), so we use the generic term.

Lithology	L 1	L 2	L 3	L 4	Reference
Sediments and sedimentary rocks					
Basaltic grains...					
... dry	×	×			Fig. 3
... wet	×	×			Fig. 3
... dry, cemented	×	×	×		Figs. 3, S10, S11
... wet, cemented	✓	✓			Figs. 3, S10
Felsic grains...					
... dry	×	×			Fig. S10
... wet	×	×			Fig. S10
... dry, cemented	×	×			Fig. S10
... wet, cemented	✓	✓			Fig. S10
Clay (smectite)...					
... dry	×	×			Fig. S10
... wet	×	×			Fig. S10
... dry, cemented	×	×			Fig. S10
... wet, cemented	×	×			Fig. S10
Cracked or porous igneous rocks					
Basalt...					
... dry	×	×	×	✓	Figs. 4, 8, 9
... wet	✓				Fig. 4
... ice-filled	×	×			Fig. 4
... dry, smectite coating	×	×	✓		Figs. 5, 7
... dry, ice coating	✓	✓			Fig. 5
... dry, gypsum coating	✓	✓	✓		Figs. 5, 7
... dry, chlorite coating	✓	✓	✓		Fig. 5, 7
... wet, smectite coating	✓				Fig. 5
... wet, ice coating	✓				Fig. 5
... wet, gypsum coating	✓				Fig. 5
... wet, chlorite coating	✓				Fig. 5
... with smectite veins	×	×	✓	✓	Figs. 8, 9
... with gypsum veins	×	×	×	×	
... with chlorite veins	×	×	×	×	
Felsic rock...					
... dry	×	×	✓		Figs. S12, 8
... wet	✓				Fig. S12
... ice-filled	×	×			Fig. S12
... dry, smectite coating	✓	✓	✓		Figs. 6, 7
... dry, ice coating	✓	✓			Fig. 6
... dry, gypsum coating	✓	✓			Fig. 6
... dry, chlorite coating	✓	✓			Fig. 6
... wet, smectite coating	✓				Fig. 6
... wet, ice coating	✓				Fig. 6
... wet, gypsum coating	✓				Fig. 6
... wet, chlorite coating	✓				Fig. 6
... with smectite veins	×	✓	✓	✓	Fig. 8
... with gypsum veins	×	×	×	×	
... with chlorite veins	×	×	×	×	
Gabbro...					
... dry	×	×	×	✓	Figs. 8, 9
... wet	✓				
... ice-filled	×	×			
... with smectite veins	×	×	✓	✓	Figs. 8, 9
... with gypsum veins	×	×	×	×	
... with chlorite veins	×	×	×	×	

provides constraints on the depth extent of the soft layer. Consistent with these observations, there is evidence for buried Noachian sediments beneath the surficial Amazonian-Hesperian lava flows at a few hundred meters depth based on layered sedimentary rocks in uplifted central peaks of large craters about 450 km to the north-east of InSight (Pan et al., 2020), which the authors suggest might extend to between 1 and 5 km depth. In addition, hundreds of meters thick stacks of layered clastic material have been observed beneath lava flows south of the landing site and might extend northward (Warner et al., 2023).

The gradual velocity increase between about 200 m and 2 km depth (Carrasco, 2024) could then be explained by compaction of the sedimentary material and an exponential decrease of porosity with depth, as shown for example in Fig. 3d). Though the rock physics models are simpler than the orbital observations in that they do not include distinct sedimentary layers, basaltic sediments as well as sediments composed of several other volcanic rock types can explain the observed velocities, as the granular properties of the material are more important than details of its composition. Although a thick layer of smectite spanning the whole depth range from 200 m to 2 km is excluded by the seismic data (Supplementary Fig. S10), thin, inter-bedded layers below the resolution of the seismic data are possible.

5.1.2. Presence of water in layer 1

Sediments in layer 1 are only compatible with the InSight velocity constraints if they are water-saturated. Thin clay layers could in this case help to retain the water within this layer. A pre-landing survey of the landing site found no evident traces of recent past or present surface interaction with water or ice (e.g. slope linea, gullies, polygonal terrain, water or ice related surface modification on steep slopes, Golombek et al., 2017). However, the study concluded that a potential Noachian global northern ocean (Clifford and Parker, 2001) would have put the landing site under water, with any water-rich deposits buried beneath 200 m of younger basalts today. Images show more than ten craters with lobate, rampart ejecta (so called “splosh” craters) that are 5 to 25 km in diameter around the InSight landing site, at distances as close as 45 km (Supplementary Fig. S16). This type of crater has been attributed to subsurface water or ice at depth (Carr et al., 1977; Barlow, 2005), which in this case would be 0.5 to 2.5 km deep (Melosh, 1989). The craters are superposed on Early Amazonian lavas and appear fresh, so they could be fairly recent.

According to thermal evolution models (Plesa et al., 2018, 2020), the presence of fluids at 1–2 km depth would only be possible for brines with a near-eutectic concentration, depending on the type of perchlorate and the corresponding melting temperature of the brine, which could be as low as 153.1 K in case of supercooled Mg perchlorate (Toner et al., 2014). The salinity of the fluids would be enhanced if the cement within the sediments was ice, since perchlorates or other salts would concentrate in the fluid phase during the onset of freezing. As little as 2 % of ice coating (and hence 98 % of fluid in the pores) would be sufficient to explain the seismic velocities, so this effect would only by minor; 10 % of ice is still consistent with the seismic constraints, though, if deposited evenly around the grain surfaces (Supplementary Fig. S17).

Some mechanism within the shallowest about 200 m beneath InSight would be required to prevent brines from rising to the surface and either freezing or evaporating, depending on perchlorate type and concentration. Given the layered shallow structure derived for the landing site (Hobiger et al., 2021; Carrasco et al., 2023a), impervious lava layers (which could be vesicular with unconnected porosity) or clays within the sedimentary layers could serve this purpose. In the Cerberus plains east of InSight, morphological analysis found evidence of recently active aqueous flood channels, with the latest flooding dated to 2–8 Ma (Burr et al., 2002). Formation of these channels requires that groundwater collected in deep aquifers. A similar aquifer might exist in the upper crust beneath InSight, but the extent of this aquifer cannot be resolved with the seismic data as they lack the required resolution for locations away from InSight.

5.1.3. Host rock of layer 2

As liquid-water saturation of larger parts of the crust is excluded by the comparatively small attenuation and high scattering (Karakostas et al., 2021; Menina et al., 2021, 2023; Stähler et al., 2024), options to model the seismic velocities in the crust below layer 1 are in general more limited. The derived velocities for layer 2 at the landing site can best be fit by dry fractured rocks with some amount of alteration. It is important to understand that we only consider rocks with cracks of a single aspect ratio in the DEM models, which is a simplification as actual rocks will contain cracks and pores with a mixture of different aspect ratios. The cracks with the lowest aspect ratios tend to dominate the effect on seismic velocities (Wilkens et al., 1991; Berge et al., 1992), while the effect of additional cracks with higher aspect ratios are comparatively minor. Hence, porosities might potentially be larger than estimated here due to additional cracks with high aspect ratios larger than the uniform value assumed here. Purely vesicular rocks without any cracks can however be excluded as the dominant aspect ratio has to be below 0.2 to fit the data (Figs. 5, 6). Another potential simplification is that we do not consider porosity to vary within the layers. This in in keeping with the constraints from the seismic data that can be modeled well by a stack of constant-velocity layers and do not require gradual changes within the layer. However, increasing pressure and increasing aspect ratios with depth for example might lead to gradual variations in seismic velocities. When considering the models for cracked rocks with alteration products partly filling the cracks, it is also important to consider that the calculated velocities are an upper bound (Supplementary Fig. S5), especially for low aspect ratios, so for a given aspect ratio, the porosities that can fit the data might actually be somewhat lower than derived here.

Since layer 2 likely consists of Noachian crust, deep and extensive fracturing by impacts can be expected, and, at the location of InSight, the ejecta from Utopia could be of special significance up to 10 km depth (Wieczorek et al., 2022), in keeping with modeling by fractured basalts (Fig. 5).

On the other hand, geochemical calculations for cooling of impact melt pools formed by large impacts on Mars suggest that deep-seated impact partial melts are buoyant in the Martian mantle and deeper crust. Thus, the ascent of ancient impact melts to neutral buoyancy levels could result in felsic layers specifically in the upper crust (Black and Marchi, 2024), and layer 2 could be modeled by fractured felsic rocks (with plagioclase as an end member, Fig. 6). Whereas InSight is not located within any known large impact basin, Black and Marchi (2024) suggest that emplacement of melt could also occur outside the actual crater and that intense bombardment during the first billion years of Mars history would lead to a dense spatial coverage by craters when also considering impactors as small as 10 km.

However, a global extent of a low-velocity upper crust equivalent to layer 2 is not supported by the InSight data, so a more localized melt emplacement due to specific impact events, e.g. Utopia, Amazonis and Deadalia, near the InSight landing site and near the S0976a bounce point would be required. Creation of felsic rocks from differentiation in impact melt sheets of several kilometer thickness has also been proposed (Koeppel et al., 2020). Cracking and alteration would in these cases need to be caused by subsequent impacts, distinct from and occurring later than the one(s) that created the felsic magmas.

Other scenarios for an ancient felsic component to the crust have also been proposed and are listed by Payré et al. (2024). Any scenarios that would result in a global - or at least regional - extent of this component, like an enriched residual melt in the late stages of a magma ocean, can likely be excluded due to the observed spatial heterogeneity in crustal velocities (Fig. 1). Scenarios that can explain variations in crustal layering on scales of a few 100 km, e.g. via melting of a heterogeneous mantle within a partial magma ocean, or re-melting due to a mantle plume, are more compatible with the observed differences in crustal velocities between the InSight landing site and other locations on Mars. Ancient volcanism that could be related to a mantle plume has however

mainly been associated with the large Tharsis volcanic province, with additional volcanic resurfacing, mainly in the Hesperian, at Elysium Mons, in the northern lowlands, and locations in the southern highlands (Broquet and Andrews-Hanna, 2023). This includes locations that should affect the surface wave paths to the north-east of InSight, but not the landing site location itself, so re-melting by a mantle plume cannot explain a felsic crustal component specifically at the landing site.

The existence of felsic rocks deeper in the crust at the landing site would be in keeping with the idea that felsic float rocks at Gale crater, about 175 km south of InSight on cratered Noachian terrain, originate from bedrock pre-dating the Gale impact and became accessible by erosion from fluvial networks that have incised 2–3 km deep (Black and Marchi, 2024), i.e. into the depth of layer 2 beneath InSight.

While fitting the constraints with a felsic rock with 23 % or more smectite veins and zero porosity is viable, the complete vanishing of crustal porosity already at 2 km depth is not expected (Hanna and Phillips, 2005; Goossens et al., 2017; De Toffoli et al., 2021). This would also imply that negligible porosity exists in deeper layers, so that cracks would have to be sealed there as well.

5.1.4. Alteration in layer 2

Alteration within layer 2, leading to coating of the cracks and fractures by hydrated minerals, could be explained by the sequestration of an ocean-scale volume of liquid water in the crust to a depth of 5–10 km, e.g. in the form of smectite, during the Noachian (Scheller et al., 2021). Indeed, under Noachian temperature conditions, smectites could have been stable to 30 km depth (DePasquale and Jenkins, 2022). Other studies suggest that smectites found in numerous Noachian outcrops rather indicate a dry climate interrupted by episodes of aqueous activity, though, as smectites deposited in the Noachian would have long since transformed diagenetically to more stable phyllosilicates like chlorite at depths as small as 300 m in the presence of liquid water (Tosca and Knoll, 2009).

Hydrological modeling suggests that ground water might have reached the surface in Elysium Planitia in Noachian times (Fassett and Head, 2008), providing a source for aqueous alteration. Formation of clay minerals deep in the crust could also have occurred by hydrothermal groundwater circulation in closed systems (Ehlmann et al., 2011), with mid-sized (Hedgepeth et al., 2024) to large basin-forming impacts, especially early in the history of Mars, creating hydrothermal conditions (Osinski et al., 2013). Given that lower-temperature phases are longest-lived in hydrothermal systems, lower temperature assemblages like smectite could result (Marzo et al., 2010).

Note that any changes in the coating material with depth, like a gradual evolution from smectite to chlorite (Sun and Milliken, 2015), would, for a constant aspect ratio, porosity, and amount of coating in the cracks, result in a gradual velocity increase that has not been resolved by the seismic data: The landing site models only allowed for constant velocities in layer 2; however, fitting all seismic data was possible within this framework (e.g. Carrasco, 2024). Modeling this kind of transition in the coating medium is also beyond the rock physics models used in this paper.

Sulphates generally occur in younger units than clays, starting in the Late Noachian (Bibring et al., 2006; Fassett and Head, 2011), and are favorably formed under more acidic water conditions that do not require the long-term presence of water (Poulet et al., 2005). They have thus been linked to precipitation from evaporating groundwater discharge, i.e. a more arid environment (Ehlmann et al., 2011). Accordingly, if sulphates are a major component of coating in any of the crustal layers, they would be expected in the upper crust.

Coating with up to 70 % of ice would be consistent with the seismic velocities, but the thermal evolution model with the greatest groundwater depth at the landing site puts this depth at 5.3 km depth (Supplementary Figs. S7, S8, Plesa et al., 2020), so ice could only be stable above this depth. It lies well within layer 2 that has a bottom depth of 8.5 to 12 km (Carrasco et al., 2023a), but a discontinuous velocity change, as expected from the transition from ice to another type of coating or even ice to liquid water, is not observed within this layer. We accordingly exclude ice as coating material (Table 2).

The azimuthal anisotropy observed in the upper-most 10 km of the crust at the landing site (Li et al., 2022b) can be explained by a subset of cracks in layer 2 that are oriented in an east-west direction and contribute 1–3.5 % of additional porosity (Supplementary Fig. S15). This is in keeping with an east-west trending stress direction in the upper crust derived from north-south oriented wrinkle ridges in western Elysium Planitia (Golombek et al., 2018, 2020) and found in models of the lithospheric stress field around the landing site (Broquet and Andrews-Hanna, 2023).

5.1.5. Comparison to previous models

Compared to the landing site models developed by Wieczorek et al. (2022), we can at least exclude the option of approximately 10 km of layered sedimentary deposits below InSight, as neither unconsolidated nor cemented sediments can fit the seismic constraints for layer 2 (Table 2). However, the uppermost about 2 km beneath the lander very likely consist of sediments. Highly fractured, altered basaltic lava, as suggested by Wieczorek et al. (2022), remains an option for layer 2, as could be ejecta from the Utopia impact, if they experienced some aqueous alteration, or layering caused by impact melt differentiation, resulting in a more felsic upper crust. However, because the layering appears to be rather localized, and higher crustal velocities are required along the raypaths both to the impact crater of event S0981c 250 km south of InSight, and to the large event S1222a, the melt differentiation is unlikely to be related to a gigantic Borealis impact, which would affect crustal structure on a larger scale, e.g. within the whole northern lowlands.

5.2. Middle crust

5.2.1. Composition at the landing site

Various scenarios can explain the velocity increase between layers 2 and 3 at the landing site (Fig. 7, Table 2). Since the velocities in layer 3 are still too small to be consistent with intact rock (Fig. 11a,b), complete closure of pores at 10 km depth, either due to elastic pore closure or viscous creep, which would result in an abrupt velocity increase (Gyalay et al., 2020), can be excluded. An increase in crack aspect ratio with depth as well as a decrease in porosity above the threshold for pore closure would likely be continuous and not marked by a single, sudden velocity increase, so a compositional contribution to this discontinuity is likely.

This could either mean a transition from more felsic material above caused by intrusions of impact partial melts to a basaltic middle crust below, or a change in the alteration products in a purely basaltic crust, e.g. from gypsum, and thus evaporation under more acidic and arid conditions in the Late Noachian, to smectite or chlorite, and thus neutral-pH alteration in the Early and Mid Noachian, or a combination of both (e.g. felsic material with gypsum coating versus basaltic material with smectite coating). The latter would also be a feasible solution in case of complete sealing of cracks by smectite. As calcite has seismic velocities similar to chlorite (Table 1), it could be considered an alternative, though carbonates are rarely detected at the surface of Mars. Since carbonate precipitation implies basic fluids (Viviano-Beck et al., 2017), this process would have happened separate in time or required a different fluid reservoir than the formation of gypsum at shallower depth, as would be the case for phyllosilicates. Recently, indications of abundant near-surface ground-water during the later Hesperian have been found in Gale crater (Banham et al., 2024), so water interaction might at least locally indeed have happened during different time intervals.

The above scenarios would all require ancient interaction with water to 20 km depth in the crust, which is in keeping with previous models of the thickness of ancient Martian aquifers (Clifford and Parker, 2001;

Hanna and Phillips, 2005). Alternatively, the velocity conditions from InSight are also met by dry cracked felsic rocks in layer 3 (Fig. 8), which would imply a larger volume of impact-derived buoyant partial melts. While compatible with models of impact-melt generation (Black and Marchi, 2024), this might be hard to reconcile with the location of InSight outside of any known large impact basin.

5.2.2. Global implications

Strikingly, a velocity increase around 20 to 25 km depth, similar to the discontinuity between layers 3 and 4 beneath InSight, is found in all velocity models derived from seismic data, with the exception of the globally averaged one (Fig. 11) that cannot resolve any crustal layering. In the middle crust, comparable in depth to layer 3, surface-wave derived velocities away from the landing site are markedly higher than below InSight, with a tendency to slightly lower values along the great circle path to S1222a than along the north-eastern great circle arcs. Due to the location uncertainty for S1222a near the dichotomy (Panning et al., 2023), this could be the equivalent of the small density contrast between the northern and southern hemispheres of Mars derived by Kim et al. (2023b). The mid-crustal velocities away from the landing site are compatible with basalt with 2 to 15 % porosity, if we consider reasonable crack aspect ratios between 0.02 and 0.1 (Supplementary Fig. S9). Alternatively, a larger amount of initial porosity and some alteration products within the cracks is also a feasible scenario, but in any case, current porosity has to be smaller than beneath InSight.

Due to the depth extent of nearly constant velocities for the models along the various great circle paths, it can be excluded that the higher velocities above 20 to 25 km depth are due to ice-filled cracks, as thermal evolution models provide maximum depth extents of the cryosphere of less than 10 km at all considered locations (Supplementary Fig. S8). Inferences on ground water cannot be made based on S-wave velocities alone, but extensive crustal aquifers can be excluded based on scattering and absorption to at least a distance of 2000 km from InSight, and specifically along the ray path to S1222a (Menina et al., 2021, 2023). The presence of fluids along part of the north-eastern great circle paths, or along the globe-circling great circle through S1222a (Fig. 1) is, on the other hand, not constrained by these studies.

Comparison of the different velocity models indicates that the low velocities at the landing site, extending over the whole crust, are exceptional (Fig. 11). Lower crustal velocities underneath InSight compared with those at other locations for which information is available is consistent with the interpretation of gravity and topography data (Gudkova et al., 2020): A local, negative free air anomaly was observed in the landing region, indicating a less dense body at this location, but not extending further to the south-east. Goossens et al. (2017) also find higher crustal densities across Elysium Mons and to the north-east of InSight than at the landing site.

A plausible cause for the unusually low velocities in the upper and middle crust at the landing site is the vicinity to large impact basins, though the extent of large impact cratering on Mars is not fully constrained, because competing geological processes could have caused degradation and burial of impact craters, even the largest ones (Melosh, 1989). During impact basin formation on Mars, the top kilometers of crust may have become excavated and overturned, while the crustal structure was altered by heating and fracturing (e.g., Branco et al., 2024), inevitably contributing to destruction and generation of porosity and crustal reworking (Wiggins et al., 2022).

Hydrocode modeling shows that a single impactor with 100 km diameter on Mars, generating a crater of about 650 km diameter, can produce porosity of up to 1 % to a depth of more than 100 km within 200 km outside of the crater radius (Wiggins et al., 2022). Modeling of the Chicxulub impact on Earth, with a crater diameter of about 180 km, predicts vast, porous and permeable regions out to 150 km from the crater center and up to 5 km deep (Alexander et al., 2024). The lower surface gravity on Mars than on Earth would result in larger regions of tensile fragmentation and porosity for the same projectile size (Wiggins et al., 2022).

The five largest Noachian impacts on Mars are significantly larger than those in the models decribed above: They could have been formed by impactors with diameters exceeding 500 km, generating craters with diameters greater than 2500 km (Roberts and Arkani-Hamed, 2012; Branco et al., 2024), which would have substantially enhanced crustal porosity to several 100 km distance outside of the crater. The InSight landing site is closer to Utopia, as well as other large basins like Isidis and Hellas (Fig. 1), than the other locations covered by the seismic measurements, so the Noachian crust at the landing site could have retained a strong influence of these large impacts through crustal fracturing and deposition of ejecta. Deposition of some hydrated minerals along the cracks could also be promoted by impact-generated hydrothermal systems (Schwenzer and Kring, 2009; Marzo et al., 2010; Osinski et al., 2013), and/or they could have been excavated from depth by the impact cratering process (Hedgepeth et al., 2024). Impact-triggered hydrothermal activity may persist for tens of thousands of years in the vicinity of the crater, with volatiles migrating along pre-existing fractures and faults, and lower-temperature assemblages, containing smectite, overprinting higher temperature phases due to the longer-lived low temperature phase of the hydrothermal system (Marzo et al., 2010). Changes in porosity and layering, even within distances of 250 km, i.e., between the InSight landing site and the location of the S0981c impact crater, are compatible with an impact cratering origin, as the severe effects of impacts on the crust decreases with radial distance from the crater.

The bounce point locations of S0976a are likewise in close vicinity of two large impacts, Amazonis and Daedalia (Roberts and Arkani-Hamed, 2012), that would influence local crustal structure. While the surface wave great circle paths also cross large Noachian impact basins or their vicinity, the crust along these paths was additionally influenced by later volcanic activity (Kim et al., 2022), e.g. at Elysium Mons and in Tharsis, and most recently in Elysium Planitia (Voigt et al., 2023; Broquet and Andrews-Hanna, 2023). Magma intrusions into the crust and the increased temperatures linked to volcanism would lead to pore closure, and might enhance deposition of hydrated minerals from hydrothermal systems, which can explain the loss of porosity and higher seismic velocities observed there.

5.2.3. Comparison to previous models

Considering the models for crustal layering discussed by Wieczorek et al. (2022), layer 3 beneath InSight could be related to fractured impact ejecta of Utopia, if the deposition of layer 2 postdates Utopia. The age of Utopia is estimated at around 4.1 Ga, whereas Hellas and Isidis are considered to be younger (Frey, 2008), and volcanic resurfacing also occurred at later times, though not preferentially at the InSight location (Broquet and Andrews-Hanna, 2023). So there might have been sufficient time in the Noachian for deposition of layer 2 on top of the Utopia ejecta. The higher velocities in layer 3 could also be caused by larger aspect ratios, a different material coating the cracks, or a larger number of cracks filled due to aqueous alteration in an ancient aquifer. However, as there are indications of liquid water at the surface specifically in ancient times, and of the ground water table reaching the surface near the landing site in the Noachian (Fassett and Head, 2008), alteration might have rather proceeded in a top-down manner (Scheller et al., 2021).

5.3. Lower crust

5.3.1. Composition at the landing site

The seismic discontinuity around 20 km depth, between layers 3 and 4 at the landing site, can be explained by pore closure and a basalt or gabbro layer with residual porosity of 1 % below, without any alteration (Table 2). From the point of view of elastic pore closure, fracture apertures might plateau at a given value as the fractal-like roughness of fracture surfaces on a microscopic scale basically decreases

compressibility to zero (Hanna and Phillips, 2005). However, this does not take viscous pore closure and plastic flow into account, which are considered the more relevant effects on Mars due to the lower gravity compared to Earth and should affect depths below about 20 km (Hanna and Phillips, 2005; Gyalay et al., 2020). A more likely scenario is thus that any porosity due to large impacts at those depths is lost due to filling with alteration products and viscous pore closure, but veins of hydrous minerals that grew along those cracks are still present and alter the seismic velocities as compared to pristine basalt or gabbro (Fig. 9e,f). In case of the mid-crust consisting of basalt with more than 19 % of cracks, or gabbro with more than 23 % of cracks, completely filled by smectite, the sudden velocity increase and the reduction of the amount of smectite-filled cracks by 50 % or more is difficult to explain.

The elastic parameters of smectite fit best with the observed velocities in layer 4; however, the present-day depth extent of layer 4 is rather compatible with higher-temperature clay polymorphs like chlorite (Sun and Milliken, 2015), though recent experimental data suggest that smectite might have been stable to 30 km depth during the Noachian (DePasquale and Jenkins, 2022). Diagenesis of chlorite from smectite can occur under a range of temperature conditions, i.e., at temperatures as low as 50° C, but requires fluids for cation exchange. Thus, the presence of smectite at depth might indicate a decreased water availability (Tosca and Knoll, 2009) after the initial clay deposition.

5.3.2. Global implications

Deep alteration occurred only locally at the landing site and is not evident on a global scale: At locations away from InSight, velocities in the lower crust are overlapping along the different surface wave great circle paths. All velocities are significantly higher than at the landing site and compatible with pristine basalt or gabbro, so either the lower crust was never affected by cracking or all cracks were closed by viscous pore closure without any alteration products being deposited along them.

5.3.3. Comparison to previous models

Note that there is an overlap in elastic parameters between basalt and gabbro, and the values chosen here for gabbro were selected to provide the maximum difference to basalt, but strictly based on seismic velocities, the two rock types are not clearly distinguishable. Accordingly, changes in crystallization alone, i.e., from basalt to gabbro between layers 3 and 4, as discussed as one possible scenario by Wieczorek et al. (2022), cannot explain the observed velocities. Pore closure below approximately 20 km depth as another suggested scenario (Wieczorek et al., 2022), on the other hand, seems likely in light of the velocities measured in other locations on Mars that are compatible with uncracked rocks, and since pore closure around 20 km depth would take less than 3.8 Ga to achieve according to thermal evolution models (Gyalay et al., 2023).

5.4. Love-Rayleigh discrepancy along the minor arc to S1222a

The model with alternating high- and low-velocity layers creating apparent anisotropy requires pristine basalt or gabbro between about 5 and 10 km depth and more damaged material above and below, whereas the additional high-velocity layer between 25 and 40 km depth is less well resolved (Xu et al., 2023). A possible explanation as outlined by Xu et al. (2023) is a maximum in loading-induced stress in the depth range between 5 and 10 km that could lead to reduced porosity as compared to surrounding regions. Modeling by Broquet and Andrews-Hanna (2023) indicates a stress field that is more homogeneous with depth at the InSight landing site than towards the east of it, which could explain why no comparable alternating layers are found beneath the lander (Knapmeyer-Endrun et al., 2021; Carrasco et al., 2023b).

Beghein et al. (2022) propose differentiation in impact melt sheets to result in layering in the crust, or inter-layering of lava flows and sediments. Similar to the differentiation of impact melt sheets, crystal preferred orientation through fractional crystallization in layered mafic intrusions has been suggested to create anisotropy in the Earth's crust (Ji et al., 2014) and would not require large-scale sedimentary layers to a depth of at least 25 km. If intrusions form in multiple episodes, they might consist of alternating olivine-rich, pyroxene-rich and plagioclase-rich layers with different seismic velocities, with addtional anisotropy due to the crystal preferred orientation of plagioclase. This type of layering occurs at crustal depth between 1.5 and 5 km and more than 50 km on Earth, with layer thicknesses of a few centimeters to a few kilometers, and spatial extents of over 50,000 km^2 (Ji et al., 2014). Its vertical scales, if below 1 km, would not be resolvable with the seismic data for the landing site.

If the anisotropy along the S1222a ray path is caused by coherent horizontal alignment of the fast axis of anisotropic minerals (Beghein et al., 2022), chlorite and serpentine are possible candidates that have been detected on Mars (Ehlmann et al., 2010). Those phyllosilicates have approximately 50 % higher S-wave velocities for polarization along the layers of SiO_4 tetrahedra than perpendicular to them, and also show 30 % or more anisotropy in P-wave velocities (Deng et al., 2022; Mookherjee and Mainprice, 2014). The observed anisotropy along the S1222a ray path would thus require some horizontal layering of phyllosilicates across the depth range between roughly 5 to at least 25 km. Studies indicate that low-concentration serpentinization, which might agree with an anisotropy significantly less than 50 % as observed here, could have been common early in Martian history (Amador et al., 2018). The density of serpentine formed under low to moderate pressure and temperature is lower than that of chlorite, around 2500 kg/m^3, and both would reduce the density of the crust as compared to basalt.

Some support for serpentinization might come from magnetic observations: Serpentinization would lead to the formation of magnetite, which could then acquire chemical remanent magnetization and act as magnetic carrier to explain Mars' remanent magnetic field (Chassefière et al., 2013; Yu and Ni, 2023). Bultel et al. (2025) found that alteration of shergottites or pyroxenites with a water-to-rock ratio of 10 could reproduce the measured magnetic field at the InSight landing site and would produce serpentine, chlorite, carbonates, and up to 0.3 to 0.4 wt% of magnetite. Along the S1222a minor arc great circle path, Gong and Wieczorek (2021) find inverted depths of magnetization between 10 and 20 km. While a depth of 10 km would correspond to a magnetized layer between the surface and 20 km depth, in keeping with the observed anisotropy, an inverted depth of 20 km would require a magnetized layer to extend significantly deeper from the surface (Gong and Wieczorek, 2021), i.e., up to the crust-mantle boundary around 60 km depth (Kim et al., 2023b). Anisotropy in the lower crust cannot be resolved by the available seismic data, so no clear conclusions regarding its depth extent and how it fits with the inverted depths of magnetization can be drawn.

A longitudinal band with chlorite and potentially serpentine signatures is found in the walls of Valles Marineris (Viviano-Beck et al., 2017); however, it is associated with observed fractures and dikes and hydrothermal alteration and might thus not be consistent with horizontal layering of the phyllosilicates. Compared to this single layer, multiple layers would need to be present to affect the depth range of at least 5 to 25 km for which anisotropy is found along the S1222a ray path. Horizontal layering of anisotropic minerals is not covered by the models considered in this study, i.e., porous or cracked rocks with vertical cracks, and which processes might create these layers over a substantial part of the crust is an open question.

5.5. Composite model for the landing site

Based on the above discussion, we combine the constraints from rock physics for the landing site, within the limits of our mineralogical and modeling assumptions (Table 2). Layer 4 consists of basalt (or gabbro) with some veins of hydrated material. This requires a process that created the cracks, e.g. the Utopia impact, and interaction with liquid

water for the deposition of hydrated minerals. Smectite is the only one of the considered alteration materials to fit the seismic constraints (Fig. 9e, f), so water must have been too limited over larger time spans to post-depostionally transform smectite into a more stable phyllosilicate like chlorite (Tosca and Knoll, 2009). Either, the cracks were completely closed by deposition of hydrated minerals, in which case the porosity could have been as low as 4 % to begin with, which would be in keeping with a decreasing amount of impact-created porosity with depth due to the relative scarcity of impacts large enough to affect lower crustal depths. Or, viscous creep closed up any remaining porosity over time. If we consider the Utopia impact as the cause of the porosity in layer 4, with a timing of about 4.1 Ga, the heat flux at later times would have been sufficient for viscous pore closure to occur at the corresponding depths for various parameter combinations of rheology, thermal conductivity and crustal heat production (Gyalay et al., 2020).

The results for layer 4 favor that layer 3 likewise consists of basalt with cracks that are partly filled by smectite: for chlorite as hydrated mineral in layer 3, higher temperatures in layer 3 than 4 during diagenesis would be required, which is unlikely, but could be the case if hydration in layer 3 is related to an impact-generated hydrothermal system. Then, porosity in layer 4 would however need to be related to a different impact-generating event and a different episode of interaction with water. Chlorite could also have been produced diagenetically from smectite, if sufficient water for cation exchange was available over prolonged time spans in layer 3, but not in layer 4. For carbonate as hydrated mineral in layer 3, a different chemistry for layer 3 as compared to layers 2 above (with either pH neutral or acidic fluids) and 4 below (with pH neutral fluids) would be necessary. For cracked plagioclase without any coating in layer 3, the absence of hydrous alteration in layer 3 would be in conflict with hydrous alteration occurring in both layer 2 above and layer 4 below.

For cracked basalt with smectite coating part of the cracks, initial porosity for reasonable ranges of crack aspect ratios at this depth would lie between 1.5 % and 24.5 %, with increasingly larger amounts of fill (from 10 % to 70 %), up to 100 % in case of porosities above 19 %. While an initial porosity in layer 3 lower than in layer 4 would not be in keeping with porosity generation by impacts, a porosity on the same order or somewhat larger would be, and require at least 30 % of pores filled by smectite. It is unlikely that impact-generated porosity alone would create a sharp contrast in velocities between layers 3 and 4, i.e., would abruptly decrease at 20 km depth, with a velocity contrast at a similar depth also observed elsewhere on Mars. While a similar porosity around 4 % in layers 3 and 4 beneath InSight and a different amount of crack filling, i.e. 100 % in layer 4 and to about 30 % in layer 3, would fit the data, the more compelling model for the abrupt velocity increase that all seismic models contain at 20–25 km depth is viscous pore closure. This would be problematic with an end-member model of 100 % of the cracks in layer 3 filled with smectite, so we consider this scenario unlikely.

Layer 2 could consist of either plagioclase or basalt with cracks and alteration. 1–3.5 % of porosity would be due to cracks with preferential east-west orientation. In the case of basalt, the alteration product would be gypsum, consistent with water interaction under more arid, Late Noachian-Hesperian conditions. Limited water availability since the Late Noachian could also explain why smectite in deeper layers did not undergo post-depositional diagenesis to chlorite (Tosca and Knoll, 2009). Like the porosity at larger depth, the porous basalt in layer 2 could likewise be the result of the Utopia impact, if it represents the deposition of impact ejecta (Wieczorek et al., 2022). In the case of plagioclase, the alteration product would be smectite (up to the point where smectite completely fills all cracks for an initial porosity above 23 %, which would however not agree with some porosity remaining in layer 3) or gypsum. The presence of cracked plagioclase would require several episodes of impact cratering, first to create felsic, buoyant melts, and then, after solidification of these melts, cracking.

Finally, shallow layer 1 consists of cemented basaltic sediments saturated with brine, with some impermeable layer to contain the fluid, and up to 10 % of the pores filled with ice as cement. The exact composition of the perchlorate in the brine cannot be determined given that each of the considered ones would reduce the melting temperature sufficiently to get liquid brine at the depth level of layer 1 beneath InSight. While Na perchlorate would have to be present in a eutectic concentration to allow for liquid brine at 200 m depth, other perchlorates could be less concentrated.

Thus, while a felsic layer in the upper crust is possible, the whole crust at the InSight landing site can also be modeled as purely basaltic. Layers roughly equivalent in depth to layers 3 and 4, though with significantly higher S-wave velocities, are also found at other locations on Mars. Away from the landing site, layer 4 could consist of basalt or gabbro without connected porosity, and layer 3 is basaltic with some porosity, though less than at the landing site, possibly with some alteration. The shallow crust away from the landing site is poorly resolved, but models are compatible with further increased porosity as compared to layer 3, similar to layer 2 beneath InSight, within the uppermost 5 km.

5.6. Implications for density and water content

Fig. 12 shows possible crustal densities compatible with the rock physics models for the InSight landing site. Due to the limited constraints on composition and porosity at other locations for which only S-

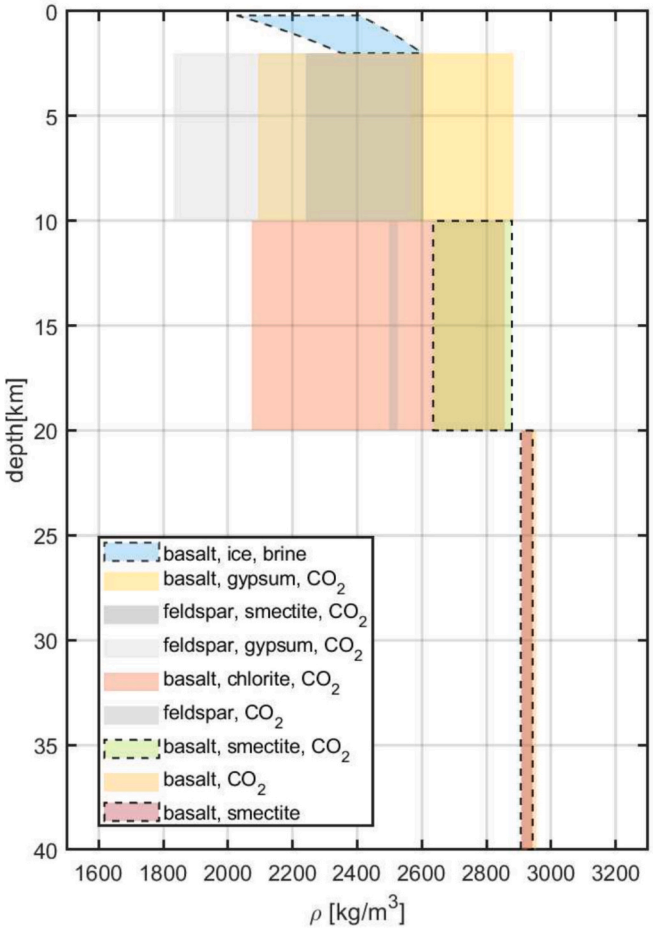

Fig. 12. Schematic density distribution in the crust for the InSight landing site based on possible compositions of different layers. For clarity of the figure, each layer is drawn with a fixed, approximate thickness here, though inversion results provide uncertainties for the layer thickness. Blocks with dashed black outline indicate the preferred model (see text), while others show alternatives. In layer 4, the ranges for basalt and CO_2 and basalt and smectite overlap almost completely.

wave velocities are available, we do not attempt to model density there. In addition to porosities that are compatible with the constraints on P- and S-wave velocities and v_P/v_S ratios, constraints on aspect ratios compatible with both porosity and depth (Supplementary Fig. S9) were taken into account.

In most cases, there is a broad overlap between the densities of different compositions considered here. All are compatible with densities around 2500 kg/m^3 in the uppermost about 10 km of the crust, consistent with the value derived by Nimmo (2002) for the upper crust from admittance analysis near the dichotomy boundary. In case of a cracked felsic crust with gypsum as alteration mineral, porosities above 10 % can be excluded because they result in densities below 2300 kg/m^3 for layer 2. In case of smectite, the range is somewhat larger, extending to roughly 20 %. On the other hand, for a basaltic crust with gypsum, porosities below 10 % lead to high densities above 2600 kg/m^3, which are also unlikely when comparing to the results of Nimmo (2002) and Goossens et al. (2017).

In layer 3, a cracked felsic rock without alteration would result in low densities that are close to those of layer 2, which is another indication that this composition is unlikely. Possible densities for basalt with cracks and chlorite coating span a large range, and porosities above 20 % can be excluded as they result in low densities below 2500 kg/m^3. In the case of cracked basalt with a smectite coating, more than 30 % coating is required, and possible porosities extend to 25 % combined with a high amount (above 50 %) of crack filling by smectite. Since the densities for basalt and gabbro from literature are identical, but the velocities of gabbro are higher (Table 1), thus requiring a larger amount of altered material, the density values for gabbro are at the lower limit of those shown for basalt for layer 4. The inclusions of altered material would make up 4–10 % of the volume in case of basalt, and 8.5–10 % in the case of gabbro, though one has to keep in mind that the velocities selected for gabbro here are at the upper limit of a plausible range.

Wernicke and Jakosky (2021) derive low, moderate and high estimates for the wt% of water required to form various hydrated minerals and mineral groups, including Fe/Mg smectites, Al smectites, chlorite and Ca sulfates, based on variable element constituents in the chemical formulas as well as a reasonable range of hydration states. We can estimate the ranges of wt% of hydrated minerals in each of the layers of our models using the various possible compositions and the densities in Table 1. For layer 4, our preferred model with 4–10 vol% of smectite as veins in basalt equates 3–8 wt% smectite, and, using the low and high estimates (Wernicke and Jakosky, 2021), between 0.3 and 3 wt% of water. For layer 3, our preferred model consists of basalt with CO_2-filled cracks partly coated by smectite. The smectite content varies between 1 and 15 wt%, equal to less than 0.1 to 6 wt% of water. The various scenarios for layer 2, either based on feldspar or basalt and with various coatings, cover a wide range between less than 0.001 and 6.5 wt% water for gypsum coating, and up to 12.9 wt% water for a felsic material with smectite coating of CO_2-filled cracks. Just considering the moderate hydration values from Wernicke and Jakosky (2021) leads to water contents of 0.7 wt% to 2 wt% in layer 4, 0.2 wt% to 3 wt% in layer 3, and 0.01 wt% to 5 wt% in layer 2.

Extrapolating from orbital detections of hydrated minerals excavated from craters, Wernicke and Jakosky (2021) derive a plausible range of 0.15 to 2.1 wt% for the water required globally to form subsurface hydrated minerals on Mars. The amount of water required for crustal hydration beneath InSight might well be within this range based on the rock physics models, but could also be larger. Due to the heterogeneity of the crust, even within 250 km distance of InSight, this local value could easily deviate from global estimates. However, lower values like those obtained for moderate hydration and scenarios without abundant smectite in layer 2 would be more consistent with a reduced availability of water since the Late Noachian-Hesperian, which could explain the prevailing existence of smectite at depth as it would prevent post-depositional diagenetic modification and would be in keeping with gypsum as hydrated mineral in layer 2.

6. Conclusions

Deriving the actual lithology from seismic data is always difficult and often ambiguous due to the variability in natural rock properties like elemental composition, porosity, and crack aspect ratio. In the case of granular material, its mechanical properties strongly depend on details of the grain contacts. This means that, usually, multiple rock physics models can fit given seismic velocities equally well. Nevertheless, with the help of additional geological observations like crater morphology and ejecta, and orbital spectral mapping, thermal evolution models, and geochemistry, seismic data from InSight can exclude some scenarios for the martian crust, specifically at the landing site where not only S-wave velocities, but also P-wave velocities and v_P/v_S ratios are independently constrained.

While we did not set out to find water in the crust, we feel nevertheless compelled to assume liquid brine as highly likely in layer 1, i.e. depths between 200 and 2000 m, beneath the lander, and also a mineralogy that would arise from earlier hydrous alteration of basaltic and/or felsic rocks in the crust below down to the crust-mantle boundary at the InSight landing site. The porosity required to make pathways for this alteration is of an amount that could be created by giant Noachian impacts, at least in the vicinity of their craters. The amount of hydrated minerals and water required could be quite low, i.e. 0.3 wt% or less of water in all layers, with minimum values decreasing towards the surface, but could also be significantly larger, indicating that crustal hydration could be an important water sink, at least locally. While a felsic contribution to the crust at the landing site is possible, the crust could also be entirely basaltic. A felsic contribution could most easily be linked to impact partial melting, and would not extend globally.

While the crustal structure at the InSight landing site is not representative for Mars in general, but likely strongly affected by its proximity to the Utopia impact crater, a discontinuity around 20 to 25 km depth is observed in seismic models for all locations on Mars and can best be explained by viscous pore closure at depth. The variability in porosity required to explain the observed lateral heterogeneity in the martian crust could be linked to magmatic processes after the initial emplacement of large-scale porosity by large impacts. As such, processes that occurred during the Noachian and Hesperian still are a major factor in shaping the present-day crust on Mars.

CRediT authorship contribution statement

Brigitte Knapmeyer-Endrun: Writing – original draft, Visualization, Software, Methodology, Investigation, Formal analysis, Conceptualization. **Ludmila Adam:** Writing – review & editing, Validation, Methodology, Formal analysis. **Sebastian Carrasco:** Writing – review & editing. **Matthew P. Golombek:** Writing – review & editing, Visualization, Validation. **Doyeon Kim:** Writing – review & editing, Validation. **Martin Knapmeyer:** Writing – review & editing, Validation, Conceptualization. **Katarina Miljković:** Writing – review & editing, Validation. **Ana-Catalina Plesa:** Writing – review & editing, Visualization, Formal analysis. **Nicholas H. Warner:** Writing – review & editing, Validation. **Mark Wieczorek:** Writing – review & editing, Validation.

Declaration of competing interest

The authors declare that they have no known competing financial interests or personal relationships that could have appeared to influence the work reported in this paper.

Acknowledgements

This is InSight Contribution Number ICN 342. We thank Catherine Johnson, Vashan Wright, and an anonymous reviewer for their

comments and suggestions that helped to improve the manuscript. A portion of this work was supported by the InSight Project at the Jet Propulsion Laboratory, California Institute of Technology under a contract with the National Aeronautics and Space Administration (80NM0018D0004). KM is fully supported by the Australian Research Council (FT210100063) and Curtin University. MW acknowledges the French Space Agency (CNES) and the French National Research Agency (ANR-14-CE36-0012-02 and ANR-19-CE31-0008-08) for funding the InSight science analysis. BKE gratefully acknowledges discussions with Lu Pan regarding hydrated minerals at the martian surface and thanks the members of the ISSI Working Group "Extant subsurface life on Mars? Science, tools & missions together", who encouraged me to think about InSight constraints on crustal porosity and hydration in detail.

Appendix A. Supplementary data

Supplementary data to this article can be found online at https://doi.org/10.1016/j.pepi.2025.107383.

Data availability

The used data are published in peer-review journals that are referenced in the text. Further information on obtaining the data is contained in the relevant publications. Details on the calculations performed are provided in the Supplementary Material, and the parameters used are given in Table 1. The Matlab code used in the calculations as well as the specific models from Carrasco et al. (2023b) used to constrain landing site velocities are available at https://doi.org/10.5281/zenodo.14739205. The event locations are taken from the Mars seismic catalogue (V14) by the InSight Marsquake Service, available at InSight Marsquake Service (2023).

References

Alexander, A.M., Marchi, S., Johnson, B.C., Wiggins, S.E., Kring, D.A., 2024. Impact-generated fragmentation, porosity, and permeability within the Chicxulub impact structure. Earth Space Sci. 11, e2023EA003383. https://doi.org/10.1029/2023EA003383.

Allo, F., 2019. Consolidating rock-physics classics: a practical take on granular effective medium models. Lead. Edge 38, 334–340.

Amador, E.S., Bandfield, J.L., Thomas, N.H., 2018. A search for minerals associated with serpentinization across Mars using CRISM spectral data. Icarus 311, 113–134. https://doi.org/10.1016/j.icarus.2018.03.021.

Amos, C., Prasad, M., Cannon, K., Dreyer, C., 2024. Velocity measurements of powdered rock at low confining pressures and comparison to Lunar shallow seismic velocity. J. Geophys. Res. Planets 129, e2024JE008287. https://doi.org/10.1029/2024JE008287.

Andrews-Hanna, J.C., Zuber, M.T., Banerdt, W.B., 2008. The Borealis basin and the origin of the Martian crustal dichotomy. Nature 453, 1212–1215. https://doi.org/10.1038/nature07011.

Arnulf, A., Singh, S., Harding, A., Kent, G., Crawford, W., 2011. Strong seismic heterogeneity in layer 2A near hydrothermal vents at the Mid-Atlantic Ridge. Geophys. Res. Lett. 38, L13320. https://doi.org/10.1029/2011GL047753.

Auzende, A.L., Pellenq, R.J.M., Devouard, B., Baronnet, A., Grauby, O., 2006. Atomistic calculations of structural and elastic properties of serpentine minerals: the case of lizardite. Phys. Chem. Miner. 33, 266–275. https://doi.org/10.1007/s00269-006-0078-x.

Bachrach, R., Avseth, P., 2008. Rock physics modeling of unconsolidated sands: accounting for nonuniform contacts and heterogeneous stress fields in the effective media approximation with applications to hydrocarbon exploration. Geophysics 73, E197–E209.

Bandfield, J.L., Hamilton, V.E., Christensen, P.R., McSween Jr., H.Y., 2004. Identification of quartzofeldspathic materials on Mars. J. Geophys. Res. Planets 109, 10009. https://doi.org/10.1029/2004JE002290.

Banerdt, W.B., Smrekar, S.E., Banfield, D., Giardini, D., Golombek, M., Johnson, C.L., Lognonné, P., Spiga, A., Spohn, T., Perrin, C., et al., 2020. Initial results from the InSight mission on Mars. Nat. Geosci. 13, 183–189.

Banham, S.G., Roberts, A.L., Gupta, S., Davis, J.M., Thompson, L.M., Rubin, D.M., Paar, G., Siebach, K.L., Dietrich, W.E., Fraeman, A.A., Vasavada, A.R., 2024. Ice? Salt? Pressure? Sediment deformation structures as evidence of late-stage shallow groundwater in Gale crater, Mars. Geology. https://doi.org/10.1130/G51849.1.

Barlow, N.G., 2005. A review of Martian impact crater ejecta structures and their implications for target properties. In: Kenkmann, T., Hörz, F., Deutsch, A. (Eds.), Large Meteorite Impacts III: Geological Society of America Special Paper 384. Geological Society of America, Boulder, CO, pp. 433–442. https://doi.org/10.1130/0-8137-2384-1.433.

Becker, A., Vrettos, C., 2016. Tests on the thermal conductivity of regolith quasi-analogues at different porosities. Earth and Space 9–15. https://doi.org/10.1061/9780784479971.002.

Beghein, C., Li, J., Weidner, E., Maguire, R., Wookey, J., Lekić, V., Lognonné, P., Banerdt, W., 2022. Crustal anisotropy in the Martian lowlands from surface waves. Geophys. Res. Lett. 49, e2022GL101508.

Belleguic, V., Lognonné, P., Wieczorek, M., 2005. Constraints on the Martian lithosphere from gravity and topography data. J. Geophys. Res. Planets 110, E11005. https://doi.org/10.1029/2005JE002437.

Berge, P.A., Fryer, G.J., Wilkens, R.H., 1992. Velocity-porosity relationships in the upper oceanic crust: theoretical considerations. J. Geophys. Res. 97, 15239–15254.

Berge, P.A., Berryman, J.G., Bonner, B.P., 1993. Influence of microstructure on rock elastic properties. Geophys. Res. Lett. 20, 2619–2622.

Berryman, J.G., 1980. Long-wavelength propagation in composite elastic media II. Ellipsoidal inclusions. J. Acoust. Soc. Am. 68, 1820–1831.

Berryman, J.G., Pride, S.R., Wang, H.F., 2002. A differential scheme for elastic properties of rocks with dry or saturated cracks. Geophys. J. Int. 151, 597–611.

Bibring, J.P., Langevin, Y., Mustard, J.F., Poulet, F., Arvidson, R., Gendrin, A., Gondet, B., Mangold, N., Pinet, P., Forget, F., et al., 2006. Global mineralogical and aqueous Mars history derived from OMEGA/Mars Express data. Science 312, 400–404. https://doi.org/10.1126/science.1122659.

Biot, M.A., 1956. Theory of propagation of elastic waves in a fluid-saturated porous solid. I. Low frequency range. J. Acoust. Soc. Am. 28, 168–178.

Black, B., Marchi, S., 2024. Buoyant impact partial melts on ancient Mars. J. Geophys. Res. Planets 129, e2023JE008040. https://doi.org/10.1029/2023JE008040.

Branco, H.C., Miljkovic, K., Plesa, A.C., 2024. New numerically derived scaling relationships for impact basins on Mars. J. Geophys. Res. Planets 129, e2023JE008217. https://doi.org/10.1029/2023JE008217.

Bridges, J.C., Catling, D., Saxton, J., Swindle, T., Lyon, I., Grady, M., 2001. Alteration assemblages in Martian meteorites: implications for near-surface processes. Space Sci. Rev. 96, 365–392. https://doi.org/10.1023/A:1011965826553.

Broquet, A., Andrews-Hanna, J.C., 2023. Geophysical evidence for an active mantle plume underneath Elysium Planitia on Mars. Nat. Astron. 7, 160–169. https://doi.org/10.1038/s41550-022-01836-3.

Bultel, B., Wieczorek, M., Mittelholz, A., Johnson, C.L., Gattacceca, J., Fortier, V., Langlais, B., 2025. Aqueous alteration as an origin of martian magnetization. J. Geophys. Res. Planets 130, e2023JE008111. https://doi.org/10.1029/2023JE008111.

Burr, D.M., Grier, J.A., McEwen, A.S., Keszthelyi, L.P., 2002. Repeated aqueous flooding from the Cerberus Fossae: evidence for very recently extant, deep groundwater on Mars. Icarus 159, 53–73.

Carr, M.H., Crumpler, L.S., Cutts, J.A., Greeley, R., Guest, J.E., Masursky, H., 1977. Martian impact craters and emplacement of ejecta by surface flow. J. Geophys. Res. 82, 4055–4065. https://doi.org/10.1029/JS082i028p04055.

Carrasco, S., 2024. Multi-Scale Investigation of the Subsurface Structure at the InSight Landing Site, on Mars, Using Single-Station Seismology. Ph.D. thesis.. University of Cologne. Urn:nbn:de:hbz:38–731699.

Carrasco, S., Knapmeyer-Endrun, B., Margerin, L., Schmelzbach, C., Onodera, K., Pan, L., Lognonné, P., Menina, S., Giardini, D., Stutzmann, E., et al., 2023a. Empirical H/V spectral ratios at the InSight landing site and implications for the Martian subsurface structure. Geophys. J. Int. 232, 1293–1310.

Carrasco, S., Knapmeyer-Endrun, B., Margerin, L., Xu, Z., Joshi, R., Schimmel, M., Stutzmann, E., Charalambous, C., Lognonné, P., Banerdt, W.B., 2023b. Constraints for the Martian crustal structure from Rayleigh waves ellipticity of large seismic events. Geophys. Res. Lett. 50, e2023GL104816. https://doi.org/10.1029/2023GL104816.

Carter, J., Poulet, F., Bibring, J.P., Mangold, N., Murchie, S., 2013. Hydrous minerals on Mars as seen by the CRISM and OMEGA imaging spectrometers: updated global view. J. Geophys. Res. Planets 118, 831–858. https://doi.org/10.1029/2012JE004145.

Chassefière, E., Langlais, B., Quesnel, Y., Leblanc, F., 2013. The fate of early Mars' lost water: the role of serpentinization. J. Geophys. Res. Planets 118, 1123–1134. https://doi.org/10.1002/jgre.20089.

Christensen, R.M., 1990. A critical evaluation for a class of micro-mechanics models. J. Mech. Phys. Solids 38, 379–404.

Clauser, C., Huenges, E., 1995. Thermal conductivity of rocks and minerals. In: Ahrens, T.J. (Ed.), Rock Physics and Phase Relations. American Geophysical Union, A Handbook of physical constants, pp. 105–126.

Clifford, S.M., Parker, T.J., 2001. The evolution of the Martian hydrosphere: implications for the fate of a primordial ocean and the current state of the northern plains. Icarus 154, 40–79. https://doi.org/10.1006/icar.2001.6671.

Compaire, N., Margerin, L., Garcia, R.F., Pinot, B., Calvet, M., Orhand-Mainsant, G., Kim, D., Lekic, V., Tauzin, B., Schimmel, M., et al., 2021. Autocorrelation of the ground vibrations recorded by the SEIS-InSight seismometer on Mars. J. Geophys. Res. Planets 126, e2020JE006498.

Dai, M., Sun, D., 2023. Martian crustal model from a joint inversion of receiver functions and apparent shear wave velocity. J. Geophys. Res. Planets 128, e2022JE007702. https://doi.org/10.1029/2022JE007702.

Dantl, G., 1968. Die elastischen Moduln von Eis-Einkristallen. Physik der kondensierten Mater. 7, 390–397.

De Toffoli, B., Massironi, M., Mazzarini, F., Bistacchi, A., 2021. Rheological and mechanical layering of the crust underneath thumbprint terrains in Arcadia Planitia, Mars. J. Geophys. Res. Planets 126, e2021JE007007.

Deng, X., Luo, C., Wentzcovitch, R.M., Abers, G.A., Wu, Z., 2022. Elastic anisotropy of lizardite at subduction zone conditions. Geophys. Res. Lett. 49, e2022GL099712. https://doi.org/10.1029/2022GL099712.

DePasquale, B.M., Jenkins, D.M., 2022. The upper-thermal stability of an iron-rich smectite: implications for smectite formation on Mars. Icarus 374, 114816. https://doi.org/10.1016/j.icarus.2021.114816.
Drilleau, M., Beucler, É., Shi, J., Knapmeyer-Endrun, B., Garcia, R.F., Kim, D., Ansan, V., Lognonné, P., Banerdt, W.B., 2023. Structure of the Martian crust below InSight from surface waves and body waves generated by nearby meteoroid impacts. Geophys. Res. Lett. 50, e2023GL104601. https://doi.org/10.1029/2023GL104601.
Dundas, C.M., Mellon, M.T., Conway, S.J., Daubar, I.J., Williams, K.E., Ojha, L., Wray, J. J., Bramson, A.M., Byrne, S., McEwen, A.S., et al., 2021. Widespread exposures of extensive clean shallow ice in the midlatitudes of Mars. J. Geophys. Res. Planets 126, e2020JE006617.
Dundas, C.M., Mellon, M.T., Posiolova, L.V., Miljković, K., Collins, G.S., Tornabene, L.L., Rangarajan, V.G., Golombek, M.P., Warner, N.H., Daubar, I.J., et al., 2023. A large new crater exposes the limits of water ice on Mars. Geophys. Res. Lett. 50, e2022GL100747. https://doi.org/10.1029/2022GL100747.
Durán, C., Khan, A., Ceylan, S., Zenhäusern, G., Stähler, S., Clinton, J., Giardini, D., 2022. Seismology on Mars: an analysis of direct, reflected, and converted seismic body waves with implications for interior structure. Phys. Earth Planet. Inter. 325, 106851.
Dvorkin, J., Nur, A., 1996. Elasticity of high-porosity sandstones: theory for two North Sea data sets. Geophysics 61, 1363–1370.
Dvorkin, J., Nur, A., 2002. Critical-porosity models. Mem. Am. Assoc. Petrol. Geol. 33–42.
Ehlmann, B.L., Edwards, C.S., 2014. Mineralogy of the Martian surface. Annu. Rev. Earth Planet. Sci. 42, 291–315. https://doi.org/10.1146/annurev-earth-060313-055024.
Ehlmann, B.L., Mustard, J.F., Murchie, S.L., 2010. Geologic setting of serpentine deposits on Mars. Geophys. Res. Lett. 37, L06201. https://doi.org/10.1029/2010GL042596.
Ehlmann, B.L., Mustard, J.F., Murchie, S.L., Bibring, J.P., Meunier, A., Fraeman, A.A., Langevin, Y., 2011. Subsurface water and clay mineral formation during the early history of Mars. Nature 479, 53–60. https://doi.org/10.1038/nature10582.
Eshelby, J.D., 1957. The determination of the elastic field of an ellipsoidal inclusion, and related problems. Proc. R. Soc. Lond. Ser. A Math. Phys. Sci. 241, 376–396.
Fassett, C.I., Head, J.W., 2008. Valley network-fed, open-basin lakes on Mars: distribution and implications for Noachian surface and subsurface hydrology. Icarus 198, 37–56. https://doi.org/10.1016/j.icarus.2008.06.016.
Fassett, C.I., Head, J.W., 2011. Sequence and timing of conditions on early Mars. Icarus 211, 1204–1214. https://doi.org/10.1016/j.icarus.2010.11.014.
Ferguson, G., McIntosh, J.C., Warr, O., Sherwood Lollar, B., Ballentine, C.J., Famiglietti, J.S., Kim, J.H., Michalski, J.R., Mustard, J.F., Tarnas, J., et al., 2021. Crustal groundwater volumes greater than previously thought. Geophys. Res. Lett. 48, e2021GL093549. https://doi.org/10.1029/2021GL093549.
Flinchum, B., Grana, D., Carr, B., Ravichandran, N., Eppinger, B., Holbrook, W., 2024. Low vp/vs values as an indicator for fractures in the critical zone. Geophys. Res. Lett. 51, e2023GL105946.
Frey, H., 2008. Ages of very large impact basins on Mars: implications for the late heavy bombardment in the inner solar system. Geophys. Res. Lett. 35. https://doi.org/10.1029/2008GL033515.
Frey, H.V., Roark, J.H., Shockey, K.M., Frey, E.L., Sakimoto, S.E., 2002. Ancient lowlands on Mars. Geophys. Res. Lett. 29, 22–1.
Garboczi, E.J., Berryman, J.G., 2001. Elastic moduli of a material containing composite inclusions: effective medium theory and finite element computations. Mech. Mater. 33, 455–470.
Garcia, R.F., Daubar, I.J., Beucler, E., Posiolova, L.V., Collins, G.S., Lognonné, P., Rolland, L., Xu, Z., Wójcicka, N., Spiga, A., Fernando, B., Speth, G., Martire, L., Rajšić, A., Miljković, K., Sansom, E.K., Charalambous, C., Ceylan, S., Menina, S., Margerin, L., Lapeyre, R., Neidhart, T., Teanby, N.A., Schmerr, N.C., Bonnin, M., Froment, M., Clinton, J.F., Karatekin, O., Stähler, S.C., Dahmen, N.L., Durán, C., Horleston, A., Kawamura, T., Plasman, M., Zenhäusern, G., Giardini, D., Panning, M., Malin, M., Banerdt, W.B., 2022. Newly formed craters on Mars located using seismic and acoustic wave data from InSight. Nat. Geosci. 15, 774–780. https://doi.org/10.1038/s41561-022-01014-0.
Gassmann, F., 1951. Über die Elastizität poröser Medien. Vierteljahrsschrift Nat. Ges. Zür. 96, 1–23.
Golombek, M., Kipp, D., Warner, N., Daubar, I.J., Fergason, R., Kirk, R.L., Beyer, R., Huertas, A., Piqueux, S., Putzig, N., et al., 2017. Selection of the InSight landing site. Space Sci. Rev. 211, 5–95. https://doi.org/10.1007/s11214-016-0321-9.
Golombek, M., Grott, M., Kargl, G., Andrade, J., Marshall, J., Warner, N., Teanby, N., Ansan, V., Hauber, E., Voigt, J., Lichtenheldt, R., Knapmeyer-Endrun, B., et al., 2018. Geology and physical properties investigations by the InSight lander. Space Sci. Rev. 214, 1–52. https://doi.org/10.1007/s11214-018-0512-7.
Golombek, M., Warner, N.H., Grant, J.A., Hauber, E., Ansan, V., Weitz, C.M., Williams, N., Charalambous, C., Wilson, S.A., DeMott, A., et al., 2020. Geology of the InSight landing site on Mars. Nat. Commun. 11, 1014. https://doi.org/10.1038/s41467-020-14679-1.
Gong, S., Wieczorek, M., 2021. Depth of Martian magnetization from localized power spectrum analysis. J. Geophys. Res. Planets 126, e2020JE006690. https://doi.org/10.1029/2020JE006690.
Goossens, S., Sabaka, T.J., Genova, A., Mazarico, E., Nicholas, J.B., Neumann, G.A., 2017. Evidence for a low bulk crustal density for Mars from gravity and topography. Geophys. Res. Lett. 44, 7686–7694. https://doi.org/10.1002/2017GL074172.
Gudkova, T., Stepanova, I., Batov, A., 2020. Density anomalies in subsurface layers of Mars: model estimates for the site of the InSight mission seismometer. Sol. Syst. Res. 54, 15–19. https://doi.org/10.1134/S0038094620010037.
Gyalay, S., Nimmo, F., Plesa, A.C., Wieczorek, M., 2020. Constraints on thermal history of Mars from depth of pore closure below InSight. Geophys. Res. Lett. 47, e2020GL088653.
Gyalay, S., Nimmo, F., Plesa, A.C., Wieczorek, M.A., Citron, R., Collins, G.S., 2023. The rise and fall of crustal porosity: Insight on early Martian history. In: 54th Lunar and Planetary Science Conference, p. 2806.
Hanna, J.C., Phillips, R.J., 2005. Hydrological modeling of the Martian crust with application to the pressurization of aquifers. J. Geophys. Res. Planets 110, E01004.
Hatakeyama, K., Katayama, I., Abe, N., Okazaki, K., Michibayashi, K., Oman Drilling Project Science Party, 2021. Effects of alteration and cracks on the seismic velocity structure of oceanic lithosphere inferred from ultrasonic measurements of mafic and ultramafic samples collected by the Oman Drilling project. J. Geophys. Res. Solid Earth 126, e2021JB021923. https://doi.org/10.1029/2021JB021923.
Heap, M.J., 2019. P-and S-wave velocity of dry, water-saturated, and frozen basalt: implications for the interpretation of Martian seismic data. Icarus 330, 11–15.
Heap, M.J., Villeneuve, M., Albino, F., Farquharson, J.I., Brothelande, E., Amelung, F., Got, J.L., Baud, P., 2020. Towards more realistic values of elastic moduli for volcano modelling. J. Volcanol. Geotherm. Res. 390, 106684.
Hearmon, R., 1984. The elastic constants of crystals and other anisotropic materials. Landolt-Bornstein Tables III/18, 1154.
Hedgepeth, J.E., Jones, E., Miljkovic, K., Branco, H.E., Plesa, A.C., 2024. Modeling the hydrothermal conditions in complex craters on Mars. In: 55th Lunar and Planetary Science Conference, p. 1786.
Hobiger, M., Halló, M., Schmelzbach, C., Stähler, S.C., Fäh, D., Giardini, D., Golombek, M., Clinton, J., Dahmen, N., Zenhäusern, G., Knapmeyer-Endrun, B., Carrasco, S., Charalambous, C., Hurst, K., Kedar, S., Banerdt, W.B., 2021. The shallow structure of Mars at the InSight landing site from inversion of ambient vibrations. Nat. Commun. 12, 6756. https://doi.org/10.1038/s41467-021-26957-7.
Hofmeister, A., 1999. Mantle values of thermal conductivity and the geotherm from phonon lifetimes. Science 283, 1699–1706.
IAPWS, 2009. Revised release on the equation of state 2006 for H2O ice Ih. In: Technical Report. The International Association for the Properties of Water and Steam. Doorwerth, The Netherlands. Http://www.iapws.org/relguide/Ice-Rev2009.pdf.
InSight Marsquake Service. Mars Seismic Catalogue, InSight Mission; V14 2023-04-01. URL. https://www.insight.ethz.ch/seismicity/catalog/v14.
Iturrino, G.J., Christensen, N.I., Kirby, S., Salisbury, M.H., 1991. 11. Seismic velocities and elastic properties of oceanic garbbroic rocks from hole 735B. In: Proceedings of the Ocean Drilling Program, Scientific Results, College Station, TX (Ocean Drilling Program), pp. 227–244.
Ji, S., Shao, T., Salisbury, M.H., Sun, S., Michibayashi, K., Zhao, W., Long, C., Liang, F., Satsukawa, T., 2014. Plagioclase preferred orientation and induced seismic anisotropy in mafic igneous rocks. J. Geophys. Res. Solid Earth 119, 8064–8088. https://doi.org/10.1002/2014JB011352.
Joshi, R., Knapmeyer-Endrun, B., Mosegaard, K., Wieczorek, M.A., Igel, H., Christensen, U.R., Lognonné, P., 2023. Joint inversion of receiver functions and apparent incidence angles to determine the crustal structure of Mars. Geophys. Res. Lett. 50, e2022GL100469. https://doi.org/10.1029/2022GL100469.
Karakostas, F., Schmerr, N., Maguire, R., Huang, Q., Kim, D., Lekic, V., Margerin, L., Nunn, C., Menina, S., Kawamura, T., Lognonné, P., Giardini, D., Banerdt, B., 2021. Scattering attenuation of the martian interior through coda-wave analysis. Bull. Seismol. Soc. Am. 111, 3035–3054. https://doi.org/10.1785/0120210253.
Katahara, K.W., 1996. Clay mineral elastic properties. In: SEG Technical Program Expanded Abstracts, pp. 1691–1694. https://doi.org/10.1190/1.1826454.
Katayama, I., Akamatsu, Y., 2024. Seismic discontinuity in the Martian crust possibly caused by water-filled cracks. Geology 52, 939–942.
Kilburn, R., Dasent, J., Wright, V., Manga, M., 2022a. Lithology, pore-filling media, and pore closure depth beneath InSight on Mars inferred from shear wave velocities. J. Geophys. Res. Planets 127, e2022JE007539. https://doi.org/10.1029/2022JE007539.
Kilburn, R., Dasent, J., Wright, V., Manga, M., 2022b. Lithology, pore-filling media, and pore closure depth beneath InSight on Mars inferred from shear wave velocities. Zenodo. https://doi.org/10.5281/zenodo.7301787.
Kim, D., Lekić, V., Irving, J.C., Schmerr, N., Knapmeyer-Endrun, B., Joshi, R., Panning, M., Tauzin, B., Karakostas, F., Maguire, R., et al., 2021. Improving constraints on planetary interiors with PPs receiver functions. J. Geophys. Res. Planets 126, e2021JE006983.
Kim, D., Banerdt, W., Ceylan, S., Giardini, D., Lekić, V., Lognonné, P., Beghein, C., Beucler, É., Carrasco, S., Charalambous, C., et al., 2022. Surface waves and crustal structure on Mars. Science 378, 417–421.
Kim, D., Duran, C., Giardini, D., Plesa, A.C., Stähler, S.C., Boehm, C., Lekić, V., McLennan, S.M., Ceylan, S., Clinton, J., et al., 2023a. Global crustal thickness revealed by surface waves orbiting Mars. Geophys. Res. Lett. 50, e2023GL103482. https://doi.org/10.1029/2023GL103482.
Kim, D., Stähler, S.C., Ceylan, S., Lekić, V., Maguire, R., Zenhäusern, G., Clinton, J., Giardini, D., Khan, A., Panning, M.P., Davis, P., Wieczorek, M., Schmerr, N., Lognonné, P., Banerdt, W.B., 2023b. Structure along the Martian dichotomy constrained by Rayleigh and Love waves and their overtones. Geophys. Res. Lett. 50, e2022GL101666. https://doi.org/10.1029/2022GL101666.
Kissick, L.E., Mather, T.A., Tosca, N.J., 2021. Unravelling surface and subsurface carbon sinks within the early Martian crust. Earth Planet. Sci. Lett. 557, 116663. https://doi.org/10.1016/j.epsl.2020.116663.
Knapmeyer-Endrun, B., Panning, M.P., Bissig, F., Joshi, R., Khan, A., Kim, D., Lekić, V., Tauzin, B., Tharimena, S., Plasman, M., et al., 2021. Thickness and structure of the Martian crust from InSight seismic data. Science 373, 438–443.
Koeppel, A.H., Black, B.A., Marchi, S., 2020. Differentiation in impact melt sheets as a mechanism to produce evolved magmas on Mars. Icarus 335, 113422. https://doi.org/10.1016/j.icarus.2019.113422.
Lemmon, E.W., Bell, I.H., Huber, M.L., McLinden, M.O., 2024. Thermophysical properties of fluid systems. In: Linstrom, P.J., Mallard, W.G. (Eds.), NIST Chemistry

WebBook. National Institute of Standards and Technology, Gaithersburg MD, 20899. NIST Standard Reference Database Number 69. https://doi.org/10.18434/T4D303 (retrieved May 29, 2024).
Lewis, K.W., Peters, S., Gonter, K., Morrison, S., Schmerr, N., Vasavada, A.R., Gabriel, T., 2019. A surface gravity traverse on Mars indicates low bedrock density at Gale crater. Science 363, 535–537. https://doi.org/10.1126/science.aat0738.
Li, J., Beghein, C., Davis, P., Wieczorek, M.A., McLennan, S.M., Kim, D., et al., 2022. Crustal structure constraints from the detection of the SsPp phase on Mars. Earth Space Sci. 10, e2022EA002416. https://doi.org/10.1029/2022EA002416.
Li, J., Beghein, C., McLennan, S.M., Horleston, A.C., Charalambous, C., Huang, Q., Zenhäusern, G., Bozdağ, E., Pike, W.T., Golombek, M., Lekić, V., Lognonné, P., Banerdt, W.B., 2022a. Constraints on the Martian crust away from the InSight landing site. Nat. Commun. 13, 7950. https://doi.org/10.1038/s41467-022-35662-y.
Li, J., Beghein, C., Wookey, J., Davis, P., Lognonné, P., Schimmel, M., Stutzmann, E., Golombek, M., Montagner, J.P., Banerdt, W.B., 2022b. Evidence for crustal seismic anisotropy at the InSight lander site. Earth Planet. Sci. Lett. 593, 117654.
Li, J., Beghein, C., Lognonné, P., McLennan, S.M., Wieczorek, M.A., Panning, M.P., Knapmeyer-Endrun, B., Davis, P., Banerdt, W.B., 2023b. Different Martian crustal seismic velocities across the dichotomy boundary from multi-orbiting surface waves. Geophys. Res. Lett. 50, e2022GL101243. https://doi.org/10.1029/2022GL101243.
Liu, Y., Wu, X., Zhao, Y.Y.S., Pan, L., Wang, C., Liu, J., Zhao, Z., Zhou, X., Zhang, C., Wu, Y., et al., 2022. Zhurong reveals recent aqueous activities in Utopia Planitia, Mars. Sci. Adv. 8, eabn8555. https://doi.org/10.1126/sciadv.abn8555.
Lognonné, P., Banerdt, W.B., Giardini, D., Pike, W.T., Christensen, U., Laudet, P., De Raucourt, S., Zweifel, P., Calcutt, S., Bierwirth, M., et al., 2019. SEIS: insight's seismic experiment for internal structure of Mars. Space Sci. Rev. 215, 1–170.
Lognonné, P., Banerdt, W.B., Pike, W., Giardini, D., Christensen, U., Garcia, R.F., Kawamura, T., Kedar, S., Knapmeyer-Endrun, B., Margerin, L., et al., 2020. Constraints on the shallow elastic and anelastic structure of Mars from InSight seismic data. Nat. Geosci. 13, 213–220.
MacKinnon, D.J., Tanaka, K.L., 1989. The impacted martian crust: structure, hydrology, and some geologic implications. J. Geophys. Res. Solid Earth 94, 17359–17370. https://doi.org/10.1029/JB094iB12p17359.
Maguire, R., Lekić, V., Kim, D., Schmerr, N., Li, J., Beghein, C., Huang, Q., Irving, J.C.E., Karakostas, F., Lognonné, P., Stähler, S.C., Banerdt, W.B., 2023. Focal mechanism determination of event S1222a and implications for tectonics near the dichotomy boundary in southern Elysium Planitia, Mars. J. Geophys. Res. Planets 128, e2023JE007793. https://doi.org/10.1029/2023JE007793.
Manga, M., Wright, V., 2021. No cryosphere-confined aquifer below InSight on Mars. Geophys. Res. Lett. 48, e2021GL093127.
Marzo, G.A., Davila, A.F., Tornabene, L.L., Dohm, J.M., Fairén, A.G., Gross, C., Kneissl, T., Bishop, J.L., Roush, T.L., McKay, C.P., 2010. Evidence for Hesperian impact-induced hydrothermalism on Mars. Icarus 208, 667–683. https://doi.org/10.1016/j.icarus.2010.03.013.
Mavko, G., Mukerji, T., Dvorkin, J., 2020. The Rock Physics Handbook, 3rd ed. Cambridge University Press. https://doi.org/10.1017/9781108333016.
Melosh, H.J., 1989. Impact Cratering: A Geological Process. Oxford University Press, New York.
Melosh, H.J., 2011. chapter 6. Impact cratering. In: Planetary Surface Processes. Cambridge University Press, Cambridge, UK, pp. 222–275.
Menina, S., Margerin, L., Kawamura, T., Lognonné, P., Marti, J., Drilleau, M., Calvet, M., Compaire, N., Garcia, R., Karakostas, F., et al., 2021. Energy envelope and attenuation characteristics of high-frequency (HF) and very-high-frequency (VF) Martian events. Bull. Seismol. Soc. Am. 111, 3016–3034.
Menina, S., Margerin, L., Kawamura, T., Heller, G., Drilleau, M., Xu, Z., Calvet, M., Garcia, R.F., Knapmeyer-Endrun, B., Carrasco, S., Onodera, K., Lognonné, P., Stott, A., Banerdt, W.B., 2023. Stratification of heterogeneity in the lithosphere of Mars from envelope modeling of event S1222a and near impacts: interpretation and implications for very-high-frequency events. Geophys. Res. Lett. 50, e2023GL103202. https://doi.org/10.1029/2023GL103202.
Mindlin, R.D., 1949. Compliance of elastic bodies in contact. J. Appl. Mech. 16, 259–268. https://doi.org/10.1115/1.4009973.
Mookherjee, M., Mainprice, D., 2014. Unusually large shear wave anisotropy for chlorite in subduction zone settings. Geophys. Res. Lett. 41, 1506–1513.
Mun, E., Kim, B., 2024. Constraining wave velocities for shallow depths on Mars. Bull. Seismol. Soc. Am. 114, 673–689. https://doi.org/10.1785/0120230040.
Murphy III, W.F., 1982. Effects of Microstructure and Pore Fluids on the Acoustic Properties of Granular Sedimentary Materials. Ph.D. thesis.. Stanford University.
Nimmo, F., 2002. Admittance estimates of mean crustal thickness and density at the Martian hemispheric dichotomy. J. Geophys. Res. Planets 107. https://doi.org/10.1029/2000JE001488, 27–1.
Norris, A., 1985. A differential scheme for the effective moduli of composites. Mech. Mater. 4, 1–16.
Nur, A., Mavko, G., Dvorkin, J., Galmudi, D., 1998. Critical porosity: a key to relating physical properties to porosity in rocks. Lead. Edge 17, 357–362. https://doi.org/10.1190/1.1437977.
Osinski, G.R., Tornabene, L.L., Banerjee, N.R., Cockell, C.S., Flemming, R., Izawa, M.R., McCutcheon, J., Parnell, J., Preston, L.J., Pickersgill, A.E., et al., 2013. Impact-generated hydrothermal systems on Earth and Mars. Icarus 224, 347–363. https://doi.org/10.1016/j.icarus.2012.08.030.
Pan, L., Ehlmann, B.L., Carter, J., Ernst, C.M., 2017. The stratigraphy and history of Mars' northern lowlands through mineralogy of impact craters: a comprehensive survey. J. Geophys. Res. Planets 122, 1824–1854. https://doi.org/10.1002/2017JE005276.
Pan, L., Quantin-Nataf, C., Tauzin, B., Michaut, C., Golombek, M., Lognonné, P., Grindrod, P., Langlais, B., Gudkova, T., Stepanova, I., Rodriguez, S., Lucas, A., 2020. Crust stratigraphy and heterogeneities of the first kilometers at the dichotomy boundary in western Elysium Planitia and implications for InSight lander. Icarus 338, 113511. https://doi.org/10.1016/j.icarus.2019.113511.
Panning, M.P., Banerdt, W.B., Beghein, C., Carrasco, S., Ceylan, S., Clinton, J.F., Davis, P., Drilleau, M., Giardini, D., Khan, A., Kim, D., Knapmeyer-Endrun, B., Li, J., Lognonné, P., Stähler, S.C., Zenhäusern, G., 2023. Locating the largest event observed on Mars with multi-orbit surface waves. Geophys. Res. Lett. 50, e2022GL101270. https://doi.org/10.1029/2022GL101270.
Pasquet, S., Bodet, L., Dhemaied, A., Mouhri, A., Vitale, Q., Rejiba, F., Flipo, N., Guérin, R., 2015. Detecting different water table levels in a shallow aquifer with combined P-, surface and SH-wave surveys: insights from Vp/Vs or Poisson's ratios. J. Appl. Geophys. 113, 38–50.
Payré, V., Salvatore, M.R., Edwards, C.S., 2022. An evolved early crust exposed on Mars revealed through spectroscopy. Geophys. Res. Lett. 49, e2022GL099639. https://doi.org/10.1029/2022GL099639.
Payré, V., Udry, A., Fraeman, A.A., 2024. Igneous diversity of the early Martian crust. Minerals 14, 452. https://doi.org/10.3390/min14050452.
Plesa, A.C., Padovan, S., Tosi, N., Breuer, D., Grott, M., Wieczorek, M., Spohn, T., Smrekar, S., Banerdt, W., 2018. The thermal state and interior structure of Mars. Geophys. Res. Lett. 45, 12–198. https://doi.org/10.1029/2018GL080728.
Plesa, A.C., Stamenković, V., Breuer, D., Hauber, E., Tarnas, J., Mustard, J., Mischna, M., De Toffoli, B., the TH2OR and VALKYRIE Teams, 2020. Mars' subsurface environment: Where to search for groundwater?. In: Europlanet Science Congress 2020 https://doi.org/10.5194/epsc2020-698 pp. EPSC2020–698.
Plesa, A.C., Wieczorek, M., Knapmeyer, M., Rivoldini, A., Walterová, M., Breuer, D., 2022. Chapter Four - Interior dynamics and thermal evolution of Mars – a geodynamic perspective. In: Schmelzbach, C., Stähler, S.C. (Eds.), Geophysical Exploration of the Solar System. Elsevier, pp. 179–230. https://doi.org/10.1016/bs.agph.2022.07.005 volume 63 of Advances in Geophysics.
Posiolova, L.V., Lognonné, P., Banerdt, W.B., Clinton, J., Collins, G.S., Kawamura, T., Ceylan, S., Daubar, I.J., Fernando, B., Froment, M., et al., 2022. Largest recent impact craters on Mars: orbital imaging and surface seismic co-investigation. Science 378, 412–417. https://doi.org/10.1126/science.abq7704.
Poulet, F., Bibring, J.P., Mustard, J., Gendrin, A., Mangold, N., Langevin, Y., Arvidson, R., Gondet, B., Gomez, C., 2005. Phyllosilicates on Mars and implications for early Martian climate. Nature 438, 623–627.
Riu, L., Carter, J., Poulet, F., 2022. The M3 project: 3–global abundance distribution of hydrated silicates at Mars. Icarus 374, 114809. https://doi.org/10.1016/j.icarus.2021.114809.
Roberts, J.H., Arkani-Hamed, J., 2012. Impact-induced mantle dynamics on Mars. Icarus 218, 278–289. https://doi.org/10.1016/j.icarus.2011.11.038.
Rubey, W.W., King Hubbert, M., 1959. Role of fluid pressure in mechanics of overthrust faulting: II. Overthrust belt in geosynclinal area of western Wyoming in light of fluid-pressure hypothesis. Geol. Soc. Am. Bull. 70, 167–206.
Sautter, V., Toplis, M.J., Beck, P., Mangold, N., Wiens, R., Pinet, P., Cousin, A., Maurice, S., LeDeit, L., Hewins, R., Gasnault, O., Quantin, C., Forni, O., Newsom, H., Meslin, P.Y., Wray, J., Bridges, N., Payré, V., Rapin, W., Le Mouélic, S., 2016. Magmatic complexity on early Mars as seen through a combination of orbital, in-situ and meteorite data. Lithos 254-255, 36–52. https://doi.org/10.1016/j.lithos.2016.02.023.
Scheller, E., Ehlmann, B., Hu, R., Adams, D., Yung, Y., 2021. Long-term drying of Mars by sequestration of ocean-scale volumes of water in the crust. Science 372, 56–62. https://doi.org/10.1126/science.abc7717.
Schimmel, M., Stutzmann, E., Lognonné, P., Compaire, N., Davis, P., Drilleau, M., Garcia, R., Kim, D., Knapmeyer-Endrun, B., Lekic, V., et al., 2021. Seismic noise autocorrelations on Mars. Earth Space Sci. 8, e2021EA001755.
Schwenzer, S.P., Kring, D.A., 2009. Impact-generated hydrothermal systems capable of forming phyllosilicates on Noachian Mars. Geology 37, 1091–1094. https://doi.org/10.1130/G30340A.1.
Shi, J., Plasman, M., Knapmeyer-Endrun, B., Xu, Z., Kawamura, T., Lognonné, P., McLennan, S.M., Sainton, G., Banerdt, W.B., Panning, M.P., Wang, T., 2023. High-frequency receiver functions with event S1222a reveal a discontinuity in the Martian shallow crust. Geophys. Res. Lett. 50, e2022GL101627. https://doi.org/10.1029/2022GL101627.
Smith, D.E., Neukum, G., Arvidson, R.E., Guiness, E.A., Slavney, S., 2003. Mars Global Surveyer Laser Altimeter Mission Experiment Gridded Data Record. Technical Report. NASA Planetary Data System, Greenbelt, Md.
Stähler, S.C., Khan, A., Giardini, D., Bagheri, A., 2024. Seismic constraints on the attenuation structure of the martian mantle. ESS Open Arch. https://doi.org/10.22541/essoar.172108303.32715707/v1.
Sun, V.Z., Milliken, R.E., 2015. Ancient and recent clay formation on Mars as revealed from a global survey of hydrous minerals in crater central peaks. J. Geophys. Res. Planets 120, 2293–2332. https://doi.org/10.1002/2015JE004918.
Tandon, G.P., Weng, G.J., 1984. The effect of aspect ratio of inclusions on the elastic properties of unidirectionally aligned composites. Polym. Compos. 5, 327–333.
Taylor, S.R., McLennan, S.M., 2009. Planetary Crusts: Their Composition, Origin and Evolution. Cambridge University Press chapter 6.3.1 SNC meteorites and crustal contamination.
Taylor, G.J., McLennan, S.M., McSween Jr., H.Y., Wyatt, M.B., Lentz, R.C.F., 2008. Implications of observed primary lithologies. In: Bell III, J.F. (Ed.), The Martian Surface: Composition, Mineralogy, and Physical Properties. Cambridge University Press, Cambridge, pp. 501–518 chapter 22.

Toner, J., Catling, D., Light, B., 2014. The formation of supercooled brines, viscous liquids, and low-temperature perchlorate glasses in aqueous solutions relevant to Mars. Icarus 233, 36–47. https://doi.org/10.1016/j.icarus.2014.01.018.

Tosca, N.J., Knoll, A.H., 2009. Juvenile chemical sediments and the long term persistence of water at the surface of Mars. Earth Planet. Sci. Lett. 286, 379–386. https://doi.org/10.1016/j.epsl.2009.07.004.

Udry, A., Howarth, G.H., Herd, C.D.K., Day, J.M.D., Lapen, T.J., Filiberto, J., 2020. What Martian meteorites reveal about the interior and surface of Mars. J. Geophys. Res. Planets 125, e2020JE006523. https://doi.org/10.1029/2020JE006523.

Vanorio, T., Prasad, M., Nur, A., 2003. Elastic properties of dry clay mineral aggregates, suspensions and sandstones. Geophys. J. Int. 155, 319–326.

Viviano-Beck, C., Murchie, S., Beck, A., Dohm, J., 2017. Compositional and structural constraints on the geologic history of eastern Tharsis Rise, Mars. Icarus 284, 43–58. https://doi.org/10.1016/j.icarus.2016.09.005.

Voigt, J.R., Hamilton, C.W., Steinbrügge, G., Christoffersen, M.S., Nerozzi, S., Kerber, L., Holt, J.W., Carter, L.M., 2023. Revealing Elysium Planitia's young geologic history: constraints on lava emplacement, areas, and volumes. J. Geophys. Res. Planets 128, e2023JE007947. https://doi.org/10.1029/2023JE007947.

Wagner, W., Pruß, A., 2002. The IAPWS formulation 1995 for the thermodynamic properties of ordinary water substance for general and scientific use. J. Phys. Chem. Ref. Data Monogr. 31, 387–535. https://doi.org/10.1063/1.1461829.

Wahl, D., Wieczorek, M.A., Wünnemann, K., Oberst, J., 2020. Crustal porosity of lunar impact basins. J. Geophys. Res. Planets 125, e2019JE006335. https://doi.org/10.1029/2019JE006335.

Walker, A.M., Wookey, J., 2012. MSAT—A new toolkit for the analysis of elastic and seismic anisotropy. Comput. Geosci. 49, 81–90.

Walsh, J.B., 1965. The effect of cracks on the compressibility of rock. J. Geophys. Res. 70, 381–389.

Warner, N.H., Golombek, M.P., Ansan, V., Marteau, E., Williams, N., Grant, J., Hauber, E., Weitz, C., Wilson, S., Piqueux, S., et al., 2022. In situ and orbital stratigraphic characterization of the InSight landing site —- a type example of a regolith-covered lava plain on Mars. J. Geophys. Res. Planets 127, e2022JE007232.

Warner, N.H., Laubenstein, A., Smearing, M., Cox, D., Golombek, M., Grant, J.A., 2023. Remnants of clastic/volcanoclastic deposits in Western Elysium Planitia, Mars: Implications for the stratigraphy beneath the InSight lander. In: 54th Lunar and Planetary Science Conference, p. 1556. https://doi.org/10.1190/1.1826454.

Werner, S.C., 2014. Moon, Mars, Mercury: basin formation ages and implications for the maximum surface age and the migration of gaseous planets. Earth Planet. Sci. Lett. 400, 54–65. https://doi.org/10.1016/j.epsl.2014.05.019.

Werner, S.C., 2019. In situ calibration of the Martian cratering chronology. Meteorit. Planet. Sci. 54, 1182–1193. https://doi.org/10.1111/maps.13263.

Wernicke, L.J., Jakosky, B.M., 2021. Martian hydrated minerals: a significant water sink. J. Geophys. Res. Planets 126, e2019JE006351. https://doi.org/10.1029/2019JE006351.

Wieczorek, M.A., Broquet, A., McLennan, S.M., Rivoldini, A., Golombek, M., Antonangeli, D., Beghein, C., Giardini, D., Gudkova, T., Gyalay, S., Johnson, C.L., Joshi, R., Kim, D., King, S.D., Knapmeyer-Endrun, B., Lognonné, P., Michaut, C., Mittelholz, A., Nimmo, F., Ojha, L., Panning, M.P., Plesa, A.C., Siegler, M.A., Smrekar, S.E., Spohn, T., Banerdt, W.B., 2022. InSight constraints on the global character of the Martian crust. J. Geophys. Res. Planets 127, e2022JE007298. https://doi.org/10.1029/2022JE007298.

Wiggins, S.E., Johnson, B.C., Collins, G.S., Melosh, J.H., Marchi, S., 2022. Widespread impact-generated porosity in early planetary crusts. Nat. Commun. 13, 4817. https://doi.org/10.1038/s41467-022-32445-3.

Wilkens, R.H., Fryer, G.J., Karsten, J., 1991. Evolution of porosity and seismic structure of upper oceanic crust: importance of aspect ratios. J. Geophys. Res. Solid Earth 96, 17981–17995.

Wilson, L., Head III, J.W., 1994. Mars: review and analysis of volcanic eruption theory and relationships to observed landforms. Rev. Geophys. 32, 221–263.

Woeber, A., Katz, S., Ahrens, T., 1963. Elasticity of selected rocks and minerals. Geophysics 28, 658–663.

Wright, V., Dasent, J., Kilburn, R., Manga, M., 2022. A minimally cemented shallow crust beneath InSight. Geophys. Res. Lett. 49, e2022GL099250. https://doi.org/10.1029/2022GL099250.

Wright, V., Morzfeld, M., Manga, M., 2024. Liquid water in the Martian mid-crust. Proc. Natl. Acad. Sci. 121, e2409983121.

Xu, Z., Broquet, A., Fuji, N., Kawamura, T., Lognonné, P., Montagner, J.P., Pan, L., Schimmel, M., Stutzmann, E., Banerdt, W.B., 2023. Investigation of Martian regional crustal structure near the dichotomy using S1222a surface-wave group velocities. Geophys. Res. Lett. 50, e2023GL103136. https://doi.org/10.1029/2023GL103136.

Yu, S., Ni, D., 2023. Serpentinisation is required for the magnetization of the Martian crust. Res. Astron. Astrophys. 23, 065012. https://doi.org/10.1088/1674-4527/accb79.

Zandt, G., Ammon, C.J., 1995. Continental crust composition constrained by measurements of crustal Poisson's ratio. Nature 374, 152–154.

Zhu, L., Kanamori, H., 2000. Moho depth variation in southern California from teleseismic receiver functions. J. Geophys. Res. Solid Earth 105, 2969–2980.